The Astrophysical Journal, 702:1393–1412, 2009 September 10 doi:10.1088/0004-637X/702/2/1393

MOIRCS DEEP SURVEY. IV. EVOLUTION OF GALAXY STELLAR MASS FUNCTION BACK TO $z \sim 3$

M. Kajisawa[1], T. Ichikawa[1], I. Tanaka[2], M. Konishi[3], T. Yamada[1], M. Akiyama[1], R. Suzuki[2], C. Tokoku[1], Y. K. Uchimoto[3], T. Yoshikawa[1], M. Ouchi[4], I. Iwata[5], T. Hamana[6], and M. Onodera[7]
[1] Astronomical Institute, Tohoku University, Aramaki, Aoba, Sendai 980–8578, Japan; kajisawa@astr.tohoku.ac.jp
[2] Subaru Telescope, National Astronomical Observatory of Japan, 650 North Aohoku Place, Hilo, HI 96720, USA
[3] Institute of Astronomy, University of Tokyo, Mitaka, Tokyo 181–0015, Japan
[4] Observatories of the Carnegie Institution of Washington, 813 Santa Barbara Street, Pasadena, CA 91101, USA
[5] Okayama Astrophysical Observatory, National Astronomical Observatory of Japan, Kamogata, Asakuchi, Okayama, 719–0232, Japan
[6] National Astronomical Observatory of Japan, Mitaka, Tokyo 181–8588, Japan
[7] Service d'Astrophysique, CEA Saclay, Orme des Merisiers, 91191 Gif-sur-Yvette Cedex, France
Received 2009 June 3; accepted 2009 July 7; published 2009 August 21

ABSTRACT

We use very deep near-infrared (NIR) imaging data obtained in MOIRCS Deep Survey (MODS) to investigate the evolution of the galaxy stellar mass function back to $z \sim 3$. The MODS data reach $J = 24.2$, $H = 23.1$, and $K = 23.1$ (5σ, Vega magnitude) over 103 arcmin^2 (wide) and $J = 25.1$, $H = 23.7$, and $K = 24.1$ over 28 arcmin^2 (deep) in the GOODS-North region. The wide and very deep NIR data allow us to measure the number density of galaxies down to low stellar mass (10^9–10^{10} $M_\odot$) even at high redshift with high statistical accuracy. The normalization of the mass function decreases with redshift, and the integrated stellar mass density becomes ∼8%–18% of the local value at $z \sim 2$ and ∼4%–9% at $z \sim 3$, which are consistent with results of previous studies in general fields. Furthermore, we found that the low-mass slope becomes steeper with redshift from $\alpha \sim -1.3$ at $z \sim 1$ to $\alpha \sim -1.6$ at $z \sim 3$ and that the evolution of the number density of low-mass (10^9–10^{10} $M_\odot$) galaxies is weaker than that of M^* ($\sim 10^{11}$ $M_\odot$) galaxies. This indicates that the contribution of low-mass galaxies to the total stellar mass density has been significant at high redshift. The steepening of the low-mass slope with redshift is an opposite trend expected from the stellar mass dependence of the specific star formation rate reported in previous studies. The present result suggests that the hierarchical merging process overwhelmed the effect of the stellar mass growth by star formation and was very important for the stellar mass assembly of these galaxies at $1 \lesssim z \lesssim 3$.

Key words: galaxies: evolution – galaxies: high-redshift – infrared: galaxies

Online-only material: color figures

1. INTRODUCTION

Understanding when and how galaxies built up their stellar mass is one of the most important issues in observational cosmology and galaxy formation. Since the stellar mass of a galaxy is generally dominated by long-lived low-mass stars, it is considered as the integral of the past star formation rate (SFR). Then, the evolution of the cosmic stellar mass density provides a global picture of the past history of star formation in the universe. Recent near-infrared (NIR) surveys allow us to measure the average stellar mass density of the universe directly from low-to-high redshift (e.g., Wilkins et al. 2008 and references therein). At $z \lesssim 1$, many previous studies found the relatively mild evolution of the average stellar mass density, although there has been a significant evolution of the relative contributions from different morphological types or different spectral energy distribution (SED)/color types to the total stellar mass density (e.g., Brinchmann & Ellis 2000; Drory et al. 2004; Bundy et al. 2005; Pannella et al. 2006; Borch et al. 2006; Franceschini et al. 2006; Vergani et al. 2008; Ilbert et al. 2009). In contrast, at $1 \lesssim z \lesssim 3$, a rapid evolution of the stellar mass density has been observed by studies based on deep surveys (Dickinson et al. 2003; Fontana et al. 2003; Fontana et al. 2004; Fontana et al. 2006; Rudnick et al. 2003, 2006; Glazebrook et al. 2004; Drory et al. 2005; Gwyn & Hartwick 2005; Arnouts et al. 2007; Pozzetti et al. 2007; Pérez-González et al. 2008), and a significant fraction of the stellar mass in the present universe seems to have been formed at that epoch. This is qualitatively consistent with results that the average SFR density in the universe peaked around $z \sim 1$–3 (e.g., Madau et al. 1996; Hopkins 2004; Hopkins & Beacom 2006), although several studies pointed out a quantitative discrepancy between the evolution of the cosmic SFR density and the stellar mass density (Rudnick et al. 2003, 2006; Hopkins & Beacom 2006; Pérez-González et al. 2008; Wilkins et al. 2008; see also Arnouts et al. 2007).

The stellar mass function (SMF) of galaxies and its evolution over cosmic time provide additional information on how stellar mass assembly of galaxies proceeded in different mass ranges, while the evolution of the integrated stellar mass density enables us to investigate when stars formed in the universe as mentioned above. In particular, the evolution of the number density of massive (e.g., $M_{\rm star} > 10^{11}$ $M_\odot$) galaxies has been extensively studied in order to address when massive galaxies assembled, which is considered as an important test for galaxy formation models (e.g., Glazebrook et al. 2004; Caputi et al. 2006; Conselice et al. 2007; Berta et al. 2007). While the comoving number density of these massive galaxies shows no significant evolution at $z \lesssim 1$, it decreases significantly with redshift at $1 \lesssim z \lesssim 3$, although the observed number density of very massive galaxies at $z \sim 2$–3 seems to be still higher than the predictions of the hierarchical galaxy formation models (Glazebrook et al. 2004; Caputi et al. 2006; Conselice et al. 2007). In order to understand how the stellar mass assembly of massive galaxies proceeded, studies for the evolution of lower mass galaxies are also important, since many low-mass objects at high redshift are expected to merge over cosmic time to form massive galaxies in hierarchical structure formation

scenarios. The hierarchical merging process generally destroys small galaxies and builds massive galaxies, and therefore this process is expected to change the shape of the SMF, for example, to increase the characteristic mass of the Schechter function and/or to flatten the low-mass slope with time. In order to address the shape of the SMF reliably, it is essential to have a large sample of galaxies over a wide range of stellar mass.

To investigate the evolution of galaxies over a wide range of mass is also important in the context of the "downsizing" scenario. In the local universe, massive galaxies tend to have redder color and older stellar population, while most low-mass galaxies are young and actively star-forming (Kauffmann et al. 2003; Brinchmann et al. 2004). The star formation histories (SFHs) of galaxies depend strongly on their stellar mass (e.g., Heavens et al. 2004; Jimenez et al. 2005). Therefore, the histories of the stellar mass assembly of high and low-mass galaxies could also be different. For example, higher SFR relative to stellar mass (i.e., specific SFR) of low-mass galaxies is expected to lead to the higher growth rate of their stellar mass than that of massive galaxies, if the effect of galaxy mergers is ignored. In fact, several studies reported that the most massive galaxies with $M_{\rm star} \sim 10^{11.5}$–$10^{12}$ $M_{\odot}$ show milder evolution in number density at $1 \lesssim z \lesssim 3$ than galaxies with $M_{\rm star} \sim 10^{11}$–$10^{11.5}$ $M_{\odot}$, i.e., the mass-dependent evolution of the number density of massive galaxies (Conselice et al. 2007; Bertone et al. 2007; Pérez-González et al. 2008). At $z \lesssim 1$–1.3, it was also observed that lower mass galaxies with $M_{\rm star} \sim 10^{10}$–$10^{11}$ $M_{\odot}$ evolve faster than massive galaxies (Fontana et al. 2006; Pozzetti et al. 2007).

However, it is difficult to extend the investigation of galaxies over a wide range of stellar mass up to $z \sim 1$–3, which is an important era in the histories of the stellar mass assembly of galaxies. This is because very deep NIR data are necessary to unbiasedly sample galaxies at high redshift down to low stellar mass, e.g., 10^{9}–10^{10} $M_{\odot}$ (Kajisawa & Yamada 2006). NIR data sample the rest-frame optical to NIR for galaxies at $z \sim 1$–3. Since NIR luminosity reflects total stellar mass of a galaxy relatively well (e.g., Bell & de Jong 2001) and is not strongly affected by dust extinction, NIR data are more suitable for construction of stellar mass limited samples than shorter wavelength data. NIR data are also important in that they straddle the redshifted Balmer/4000 Å break of these high-z galaxies, which is correlated strongly with the stellar M/L ratio and enables us to estimate stellar mass with high accuracy. Since such deep NIR data have been very limited so far, only a few studies investigated the evolution of the shape of the SMF up to $z \sim 1$–3 using ultra-deep NIR data with relatively small survey areas (Gwyn & Hartwick 2005; Marchesini et al. 2009).

In this paper, we use very deep and wide NIR data obtained in MOIRCS Deep Survey (MODS; Kajisawa et al. 2006; Ichikawa et al. 2007) with publicly available multiwavelength data in the Great Observatories Origins Deep Survey (GOODS; Giavalisco et al. 2004) in order to investigate the evolution of the SMF of galaxies back to $z \sim 3$. The wide and deep NIR data allow us to construct a statistically large galaxy sample over a wide range of stellar mass even at high redshift. Section 2 describes the data set and the procedures of source detection and photometry. We present methods for constructing the SMF and investigate its evolution in Section 3. In Section 4, we compare the results with previous studies and discuss their implications for galaxy formation and evolution. A summary is provided in Section 5.

We use a cosmology with $H_0 = 70$ km s^{-1} Mpc^{-1}, $\Omega_{\rm m} = 0.3$ and $\Omega_{\Lambda} = 0.7$. The Vega-referred magnitude system is used throughout this paper.

2. OBSERVATIONAL DATA AND SOURCE DETECTION

In the MODS, we obtained the very deep *JHK*-bands imaging data in the field of GOODS-North with Multi-Object InfraRed Camera and Spectrograph (MOIRCS; Ichikawa et al. 2006; Suzuki et al. 2008) mounted on the Subaru Telescope. The observations were carried out in the period from 2006 April to 2008 May. We also used archival MOIRCS data obtained by Wang et al. (2009) and Bundy et al. (2009). Four MOIRCS pointings cover ∼70% of the GOODS-North region (∼ 103.3 arcmin^2, hereafter referred as "wide" field) and the total exposure time is 6.3–9.1 hr in J band, 2.5–4.3 hr in H band and 8.3–10.7 hr in K band. One of the four pointings, which includes the Hubble Deep Field North (HDF-N, Williams et al. 1996), is also the ultra-deep field of the MODS (hereafter "deep" field), where the exposure time is 28.2 hr in J band, 5.7 hr in H band, and 28.0 hr in K band.

The data were reduced using a purpose-made IRAF-based software package called MCSRED.[8] The reduction procedures were as described in Kajisawa et al. (2006) except that a defringing process was additionally applied. A standard star P177-D (Leggett et al. 2006) was used for flux calibration. In a photometric night, object frames for flux calibration were observed immediately after the standard star at similar air mass in all four pointings in *JHK* bands. Before combining the object frames, all frames were scaled to the count level of these calibration frames using relatively bright unsaturated sources. We discarded the frames where the count level was very low (less than 70% of the calibration frame) or the image quality was bad (full width at half-maximum (FWHM) of the PSF larger than 1.2 arcsec for the wide field and 0.8 arcsec for the deep field). The combined data reach $J = 24.2$, $H = 23.1$, and $K = 23.1$ (5σ, Vega magnitude) for the wide field and $J = 25.1$, $H = 23.7$, and $K = 24.1$ for the deep field. Further details of the observations, reduction, and quality of the data will be presented in a forthcoming paper (M. Kajisawa et al. 2009, in preparation).

The source detection was performed in the K-band image using the SExtractor image analysis package (Bertin & Arnouts 1996). We adopted MAG_AUTO from the SExtractor as the total K-band magnitudes of the detected objects. In this study, we use the magnitude-limited samples with $K < 23$ and $K < 24$ for the wide and deep fields, respectively. The detection completeness for point sources is more than 90% at the K-band limits in both the samples, and the false detection rate is expected to be less than ∼ 1% from the simulation of the source detection on the inverse K-band image with the same detection parameters (M. Kajisawa et al. 2009, in preparation). We detected 6402 and 3203 sources above the K-band limits in the wide and deep fields, respectively.

In order to measure the optical-to-MIR SEDs of the detected objects, we used the publicly available multiwavelength data in the GOODS field, namely KPNO/MOSAIC (U band, Capak et al. 2004), *Hubble Space Telescope*/Advanced Camera for Surveys (*HST*/ACS; B, V, i, z bands, version 2.0 data; M. Giavalisco et al. 2009, in preparation; Giavalisco et al. 2004) and *Spitzer*/IRAC (3.6 μm, 4.5 μm, 5.8 μm, DR1, and DR2; M.

[8] http://www.naoj.org/staff/ichi/MCSRED/mcsred_e.html

Dickinson et al. 2009, in preparation), as well as the MOIRCS *J*- and *H*-bands images. These multiband images were aligned to the *K*-band image. The ACS and MOIRCS images were convolved to match the data with the poorest seeing for both the wide (to $\sim$ 0.6 arcsec FWHM) and deep (to $\sim$ 0.5 arcsec FWHM) samples. For the color measurements, we used a fixed aperture size with a diameter of 1.2 (1.0 for the deep sample) arcsec ($\sim$ 2$\times$seeing FWHM) for the ACS and MOIRCS data. For MOSAIC (*U* band) and IRAC (3.6 μm, 4.5 μm, and 5.8 μm) data, we first performed the aperture photometry of the wide (deep) sample with aperture sizes of 2.28 (2.39), 2.89 (3.07), 3.05 (3.24), 3.80 (4.02) arcsec, respectively, and then applied the aperture correction by using the light profiles of the *B*- and *K*-bands images smoothed to match the resolution of *U*-band and IRAC images, respectively (see M. Kajisawa et al. 2009, in preparation for details).

In the following analysis, we use objects which are detected above 2σ level in more than three bands (*K* band and other two bands) because it is difficult to estimate the photometric redshift and stellar mass of those detected only in one or two bands. In the wide and deep *K*-band magnitude-limited samples, only 21/6402 and 42/3203 were excluded by this criterion, respectively. As a result, the wide and deep samples consist of 6381 and 3161 objects, respectively, and the total number of objects used are 7563, in which 1979 objects with $K < 23$ in the deep field are included in both the samples.

3. ANALYSIS

3.1. Estimate of Redshift and Stellar Mass

In order to estimate the photometric redshift and stellar mass of the sample galaxies, we performed SED fitting of the multiband photometry described above (*UBVizJHK*, 3.6 μm, 4.5 μm, and 5.8 μm) with population synthesis models. We adopted the standard minimum χ^2 method for the fitting procedure. The resulting best-fit redshift (i.e., photometric redshift) is used for objects without spectroscopic identifications and the best-fit stellar mass-to-luminosity (M/L) ratio is used to calculate the stellar mass. We adopted spectroscopic redshifts (if available) from the literature (Cohen et al. 2000; Cohen 2001; Dawson et al. 2001; Wirth et al. 2004; Cowie et al. 2004; Treu et al. 2005; Chapman et al. 2005; Reddy et al. 2006a; Barger et al. 2008), including those from our NIR spectroscopic observation of $\sim$ 20 star-forming *BzK* galaxies (Daddi et al. 2004) at $z \sim 2$ with Subaru/MOIRCS (T. Yoshikawa et al. 2009, in preparation). For these objects, the SED fitting was performed fixing the redshift to each spectroscopic value.

In this study, three models, i.e., GALAXEV (Bruzual & Charlot 2003), PEGASE version 2 (Fioc & Rocca-Volmerange 1997), and Maraston (2005) model, were used as SED templates. Comparisons among the results with different SED template sets allow us to check the systematic effects of these models on the estimate of redshift and stellar mass. We also used a public photometric redshift code, EAZY (Brammer et al. 2008) for an independent check of the photometric redshift. In all SED models, Salpeter IMF (Salpeter 1955) with lower and upper mass limits of 0.1 and 100 $M_\odot$ is adopted for easy comparison among the results with the models and those in other studies. The details of the model templates from each population synthesis model are given in the following.

1. *GALAXEV*. We used the similar template sets described in Kajisawa & Yamada (2005). Exponentially decaying SFHs with the decaying timescale τ ranging between 0.1 and 20 Gyr are assumed. Calzetti extinction law (Calzetti et al. 2000) in the range of $E(B-V) = 0.0$–1.0 is adopted. Metallicity is changed from 1/50 to 1 solar metallicity.
2. *PEGASE2*. We used the same template sets as those described in Grazian et al. (2006). Eight exponentially decaying SFHs with various gas infalling and SFR timescales are assumed ($\tau_{\rm gas} = 0.1$–5 Gyr and $\tau_{\rm SFR} = 0.1$–20 Gyr; see Table 4 in Grazian et al. 2006 for details). The model includes the metallicity evolution and dust extinction in a self-consistent way. Following Grazian et al. (2006), we also added passively evolving templates with a constant SFR and several truncation ages, and dusty star-forming templates with a constant SFR and the Calzetti extinction with the range of $E(B-V) = 0.5$–1.1.
3. *Maraston (2005)*. The same SFHs and the same range of the Calzetti extinction as in the case of GALAXEV are assumed ($\tau = 0.1$–20 Gyr and $E(B-V) = 0.0$–1.0). Metallicity is changed from 0.5 to 2.0 solar metallicity. This model increases emphasis on contributions of thermally pulsating AGB stars to the SEDs. In all these 1–3 models, the model age is changed from 50 Myr to the age of the universe at the observed redshifts. We also added to the model SEDs the Lyman series absorption produced by the intergalactic medium following Madau (1995).
4. *EAZY*. We used the default parameter setting and the default template set of *eazy_v1.0*. The default template set consists of five principal component templates constructed from a large number of PEGASE models that cover a distribution of the SFH of galaxies in the semi-analytic model by De Lucia & Blaizot (2007). In addition to these principal components, a dusty star-forming SED is added as a complementary template. EAZY fits the multiband photometry of the observed galaxies with a linear combination of these templates (see Brammer et al. 2008 for details). Since EAZY fits with the templates based on the principal components, we cannot derive the precise stellar M/L ratio from the fitting procedure. In order to estimate the stellar mass, therefore, we performed SED fitting with the 1–3 models, fixing the redshift to the output from EAZY. The results with the different population synthesis models at the same redshifts also enable us to check the systematic effect of these models on the estimate of stellar M/L ratio independently.

In Figure 1, we compare the photometric redshifts with a sample of 2102 spectroscopic redshifts from the literature described above. The photometric redshift accuracy and the fraction of the catastrophic failure with $\delta z/(1+z_{\rm spec}) > 0.5$ for each SED model are ($\delta z/(1+z_{\rm spec}) = -0.009 \pm 0.077$, 4.0% outliers) for GALAXEV, (-0.002 ± 0.103, 4.0%) for PEGASE2, (-0.007 ± 0.082, 3.9%) for the Maraston model, and ($+0.003 \pm 0.098$, 4.7%) for EAZY, respectively. Although the photometric redshift accuracy is relatively good in all cases, there are some systematic differences among the models especially at $1.5 < z < 3.0$ in Figure 1. We check the effects of these differences of the photometric redshifts on the SMF in Section 3.4.

Table 1 lists the number of objects in each redshift bin for different SED models. These redshift bins, of which width is sufficiently larger than the typical photometric redshift errors, were defined so as to include a reasonable number of galaxies in the bin for calculating the SMF. The comoving volumes are 8.5×10^4 Mpc^3 (2.5×10^4 Mpc^3 for the deep field) at $0.5 < z < 1.0$, 1.4×10^5 Mpc^3 (3.7×10^4 Mpc^3) at $1.0 < z < 1.5$, 3.4×10^5 Mpc^3 (9.2×10^4 Mpc^3) at $1.5 < z < 2.5$, and 3.4×10^5 Mpc^3

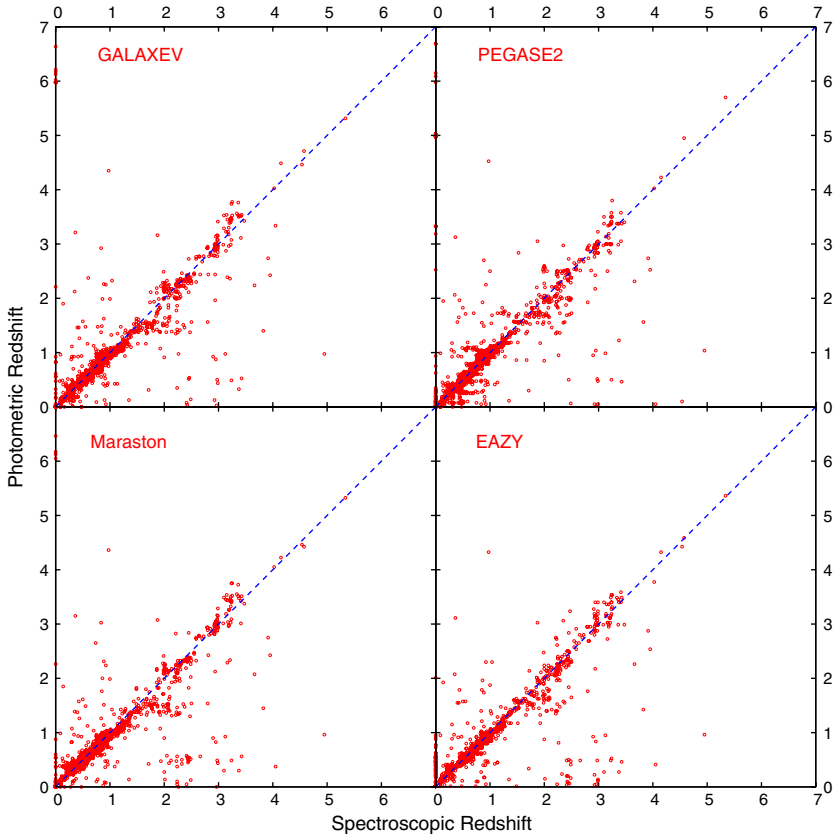

Figure 1. Photometric redshift vs. spectroscopic redshift for galaxies with spectroscopic redshifts from the literature. Four panels show the different population synthesis models used as SED templates in the photometric redshift estimate.

(A color version of this figure is available in the online journal.)

Table 1
Sample Size in Each Redshift Bin

Redshift	Model Templates	Wide ($K < 23$, 103 arcmin^2)[a]	Deep ($K < 24$, 28 arcmin^2)[a]
z =0.5–1.0	GALAXEV	1945 (859)	902 (311)
	PEGASE2	1860 (859)	836 (311)
	Maraston	2118 (859)	1023 (311)
	EAZY	2141 (859)	991 (311)
z =1.0–1.5	GALAXEV	1426 (353)	635 (105)
	PEGASE2	1319 (353)	608 (105)
	Maraston	1403 (353)	573 (105)
	EAZY	1141 (353)	464 (105)
z =1.5–2.5	GALAXEV	1306 (209)	666 (75)
	PEGASE2	1380 (209)	677 (75)
	Maraston	1015 (209)	488 (75)
	EAZY	1334 (209)	774 (75)
z =2.5–3.5	GALAXEV	487 (95)	366 (57)
	PEGASE2	507 (95)	370 (57)
	Maraston	427 (95)	302 (57)
	EAZY	494 (95)	356 (57)

Note. [a] Number in the parenthesis indicates objects with spectroscopic redshift.

(9.3×10^4 Mpc^3) at $2.5 < z < 3.5$, respectively. The parenthesis in Table 1 represents the number of objects with spectroscopic redshift. The fraction of spectroscopically identified sources is relatively high, thanks to the extensive spectroscopic surveys in this field.

As discussed in previous studies (e.g., Papovich et al. 2001; Kajisawa & Yamada 2005; Shapley et al. 2005), the uncertainty of the stellar mass is smaller than other parameters such as stellar age, star formation timescale, metallicity, and dust extinction. While the broadband SEDs are degenerated with respect to these parameters of the stellar populations (stellar age, star formation timescale, metallicity, and dust extinction), the stellar M/L ratio (and therefore stellar mass) is much less affected by the degeneracy because the effects of these parameters on the stellar M/L ratio tend to be canceled out with each other. Figure 2 shows the uncertainty of the stellar mass estimated from a χ^2 map in SED fitting with the GALAXEV model for each object. For sources without spectroscopic identifications, we also varied

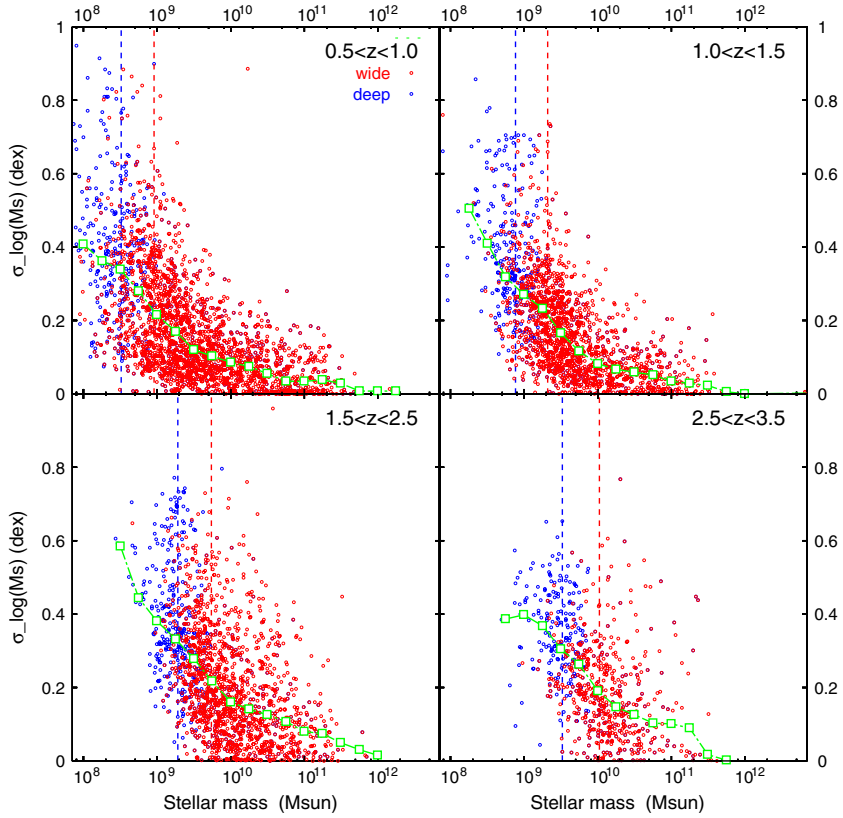

Figure 2. Uncertainty of the estimated stellar mass as a function of stellar mass in each redshift bin. Red circles represent the wide sample and blue circles show the deep sample. Vertical dashed lines show the limiting stellar mass described in the text for the wide (red) and deep (blue) samples, respectively. Open squares represent the median values at each stellar mass for all sample. For objects without spectroscopic redshift, the photometric redshift error is taken into account in the estimate of stellar mass uncertainty (see the text).

(A color version of this figure is available in the online journal.)

redshift as a free parameter in the calculation of the χ^2 map to take into account the photometric redshift error. The uncertainty increases with decreasing stellar mass and increasing redshift. The stellar mass errors become $\sim$ 0.3–0.4 dex at the limiting stellar mass (the vertical dashed lines in the figure) described in the following subsection.

3.2. Stellar Mass-limited Sample

The K-band magnitude-limited sample does not have a sharp limit in stellar mass even at a fixed redshift, because the stellar M/L ratio at the observed K band varies with different stellar populations. We used the rest-frame $U-V$ color distribution as a function of stellar mass in each redshift bin to estimate the limiting stellar mass above which most of the galaxies are expected to be brighter than the magnitude limits and detected in the K-band image. Since rest-frame $U-V$ is correlated with stellar M/L ratio (e.g., Rudnick et al. 2003; Marchesini et al. 2007), one can predict the mass dependence of stellar M/L and then estimate the effect of the magnitude limit on the stellar mass distribution.

Figure 3 shows the rest-frame $U-V$ distribution in each redshift bin for the wide sample (top panels) and the deep sample (middle panels). A dashed line in each panel represents the K-band magnitude limit ($K = 23$ for the wide sample and $K = 24$ for the deep one). All objects with stellar mass larger than this line (on the right side of the line in the figure) at each $U-V$ value are brighter than the magnitude limit. In order to calculate the line, we used the stellar M/L ratio and the rest-frame color of the GALAXEV model with various SFHs, dust extinction, and metallicity. The maximum mass was selected from the possible range of the stellar mass for the models with $K = 23$ (or 24 for the deep sample) and each $U-V$ color in order to depict the dashed line in the figure. Dashed-dot lines in Figure 3 represent the 90 percentile of $U-V$ color at each stellar mass. We adopted the point where the lines of the magnitude limit and 90 percentile of $U-V$ color cross each other as the limiting stellar mass. Above this limiting mass, more than 90% of objects are expected to be brighter than the K-band magnitude limit.

The bottom panels in Figure 3 show the comparison of the 90 percentiles of $U-V$ color for the wide and deep samples. The 90 percentiles for both the samples agree well with each other even near the limiting mass of the wide sample. This suggests that the incompleteness near the magnitude limit of the wide sample does not strongly affect the $U-V$ color distribution, although some red galaxies might be missed on the left-hand side of the long-dashed line.

Figure 4 shows the calculated limiting stellar mass as a function of redshift for the wide and deep samples. We also estimated these mass limits for the cases with PEGASE2 and Maraston models as well as the case with GALAXEV. As seen in Figure 3 and other previous studies (e.g., Kajisawa & Yamada 2005; Kajisawa & Yamada 2006; Labbé et al. 2005; Taylor et al. 2009), less massive galaxies tend to have bluer rest-frame color even at high redshift. Such a mass-dependent color distribution can be seen well above the K-band magnitude limit up to at

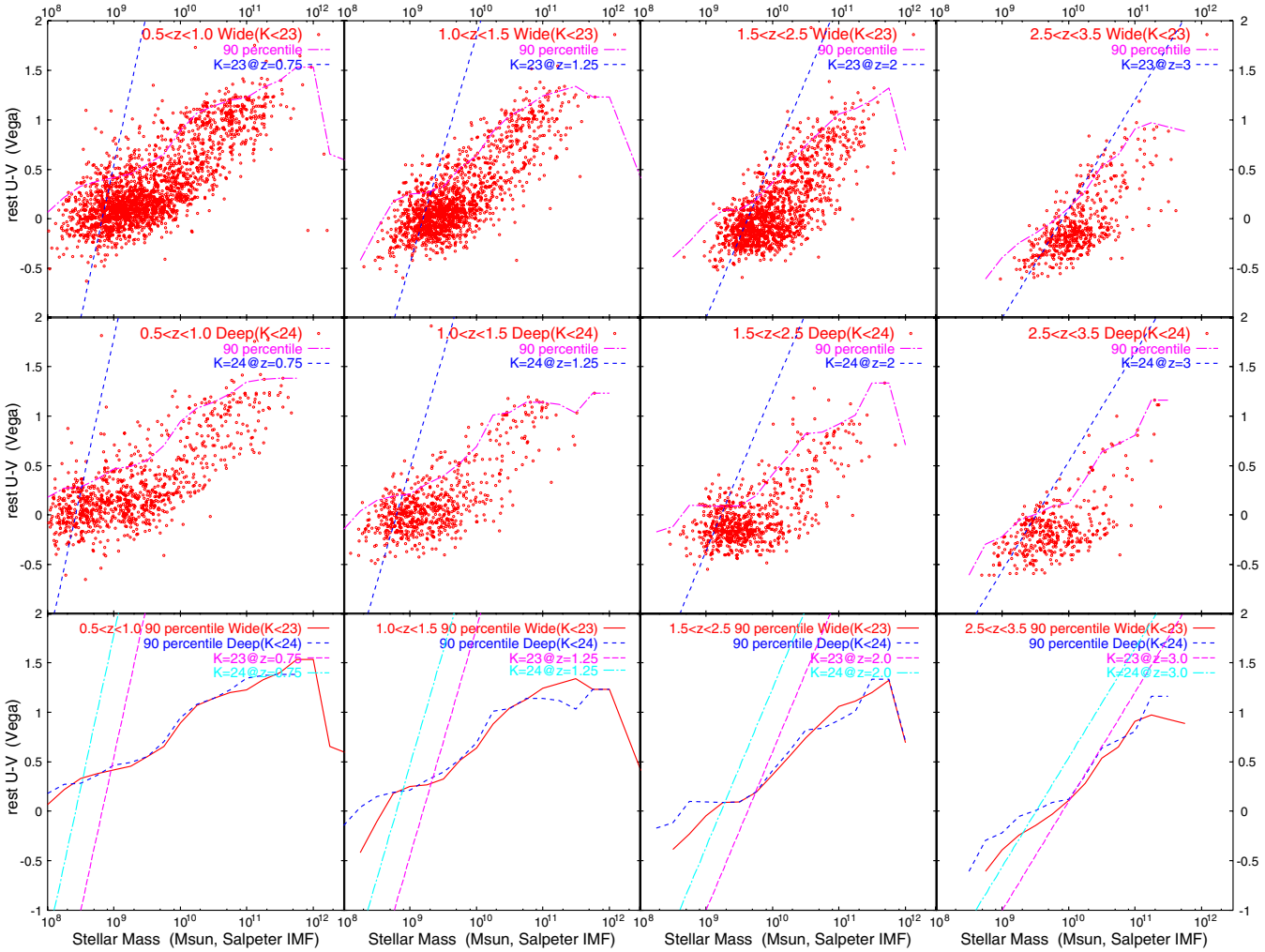

Figure 3. Top and middle: rest-frame $U-V$ color distributions of wide (top) and deep (middle) samples for each redshift bin. Dashed lines represent the K-band magnitude limits ($K = 23$ for the wide sample and $K = 24$ for the deep one) at the central redshift of each bin. Dashed-dot curves show the 90 percentile of $U-V$ color at each stellar mass. Bottom: comparison of the 90 percentile of $U-V$ color between the wide (solid line) and deep (short dashed line) samples. Long-dashed line and dashed-dot line show the K-band magnitude limits for the wide and deep samples.

(A color version of this figure is available in the online journal.)

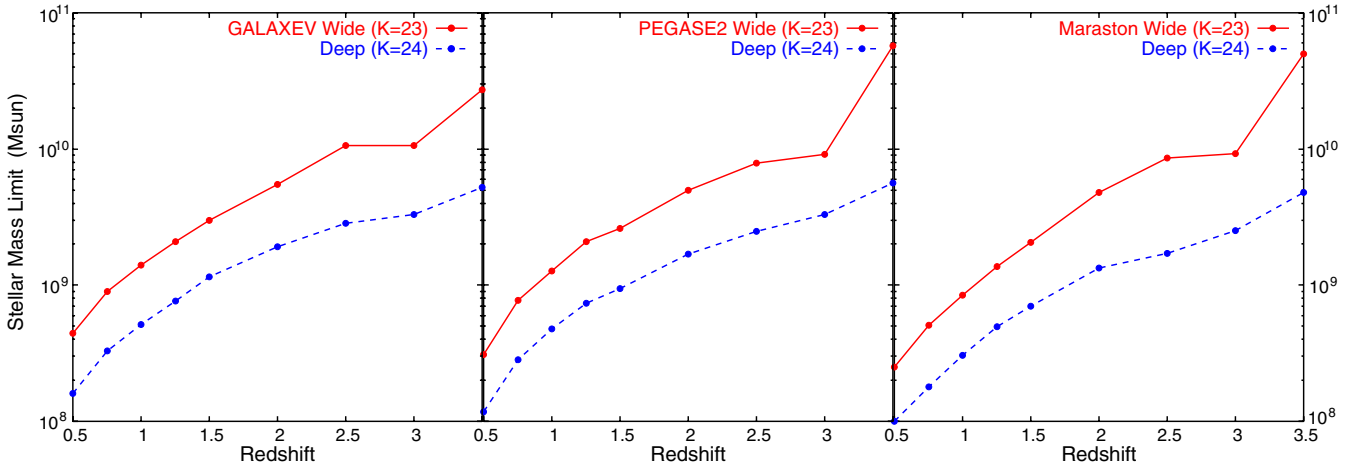

Figure 4. Stellar mass limit as a function of redshift for the wide and deep samples. Three panels show the results with the different SED models. Solid lines show the wide sample and dashed lines show the deep one.

(A color version of this figure is available in the online journal.)

least $z \sim 2.5$ in Figure 3. Since the bluer color of low-mass galaxies indicates a lower M/L ratio, we can detect galaxies down to the relatively lower mass limit with high completeness compared with, for example, the mass limit based on the M/L

ratio of the passively evolving models, which is used in other previous studies (e.g., Dickinson et al. 2003; Fontana et al. 2004). On the other hand, our "wide" field data are relatively shallow for galaxies at $z > 3$ (top right panel in Figure 3) and the completeness is relatively low even at high mass, where galaxies tend to have red rest-frame colors (high M/L ratios). We use objects with the stellar mass larger than these mass limits at each redshift to estimate and discuss the SMF in the following.

3.3. Deriving the Stellar Mass Function

The SMF of galaxies was derived with the non-parametric $1/V_{\rm max}$ formalism and the parametric STY method (Sandage et al. 1979). Both methods are commonly used to estimate the luminosity function and SMF of galaxies.

In the $V_{\rm max}$ method, $V_{\rm max}$ was calculated with the best-fit model SED template for each galaxy. For each best-fit SED, we estimated the K-band apparent magnitude as a function of redshift, taking into account both the luminosity distance and K correction. Then we determined the maximum redshift, $z_{\rm max}$ above which the object becomes fainter than the K-band magnitude limit ($K = 23$ for the wide sample or $K = 24$ for the deep sample). $V_{\rm max}$ is a comoving volume integrated from the lower limit of each redshift bin to $z_{\rm max}$ or the upper limit of the bin (the smaller of these two). Then $1/V_{\rm max}$ estimates were used to calculate the number density of galaxies in each mass bin.

In the STY method, assuming the Schechter function form (Schechter 1976) for the SMF, we estimated best-fit values of the Schechter parameters (α, M^*, ϕ^*). The limiting stellar mass $M_{\rm lim}(z)$ (described in the previous subsection) for the redshift of each object was used to calculate the probability that the object has the observed stellar mass M as

$$p = \frac{\phi(M)}{\int_{M_{\rm lim}(z)}^{\infty} \phi(M) dM}. \quad (1)$$

Here $\phi(M)$ is the SMF represented by the Schechter function. We searched for the values of the Schechter parameters (α, M^*, ϕ^*) which maximize the likelihood $L = \prod p$, the products of the probability densities for the objects with the stellar mass larger than $M_{\rm lim}(z)$ in each redshift bin. Both the wide and deep samples were used simultaneously in the maximum likelihood technique.

3.4. Evolution of the Stellar Mass Function

Figure 5 shows the SMF of galaxies in the different redshift bins for the different SED models. The results of the $V_{\rm max}$ method and the best-fit Schechter function estimated with the STY method are plotted in each panel. Error bars are based on the Poisson statistics. Dashed lines show the local SMF derived from the 2dF and Two Micron All Sky Surveys (Cole et al. 2001) with the small correction for the "maximum age" method as described in Fontana et al. (2004). In Figure 6, we plot the combined wide and deep complete data (same as the solid symbols in Figure 5) for the different SED models with different symbols in the same panel.

Figures 5 and 6 show that the SMFs obtained from different samples and SED models are in good agreement, although there are some systematic differences among the SMFs. The number densities for the deep sample are systematically larger (by $\sim$ 0.1 dex) than those for the wide sample at $0.5 < z < 1.0$ for all SED models. Our deep field is centered at the HDF-N field where the extensive spectroscopic surveys revealed the large-scale structures at $z = 0.85$ and $z = 1.02$ (Cohen et al. 2000; Wirth et al. 2004). These filaments or clumps around the HDF-N could cause the slightly larger number density in our deep field, and such differences can be considered as the possible field-to-field variance. Slighter excess in the deep field can also be seen at $2.5 < z < 3.5$ in most SED-model cases, and this may also be due to large-scale structures. On the other hand, the systematic differences among the different SED models in Figure 6 seem to be larger. The number density of galaxies for the Maraston model is systematically smaller by $\sim$ 0.15–0.2 dex (up to $\sim$ 0.5 dex at $> 10^{11}$ $M_\odot$) than those for the GALAXEV and PEGASE2 models especially at $z > 1.5$. Since the differences are also seen between the EAZY+Maraston and EAZY+GALAXEV/PEGASE2, where the same redshifts of EAZY are used, the differences of the estimated stellar M/L ratio among the SED models cause the systematic differences of the number density. For example, Maraston et al. (2006) performed the broadband SED fitting of relatively young ($\sim$ 0.2–2 Gyr stellar age) galaxies at $1.4 < z < 2.7$ with the Maraston and GALAXEV models and reported that the Maraston model gives systematically younger age and lower stellar mass ($\sim$ 60%) than the GALAXEV model. Such difference of the estimated stellar mass seems to explain the differences seen in Figure 6. If the fraction of young galaxies becomes larger at high redshift, the larger differences in the SMFs at $z > 1.5$ could also be explained because the contribution of TP-AGB stars is expected to be significant in the relatively young ages ($\sim$ 0.2–2 Gyr, Maraston 2005; Maraston et al. 2006).

We can see general evolutionary features in Figures 5 and 6 in spite of the field variance and the systematic differences among the SED models mentioned above. We note, first, that the overall number density decreases gradually with redshift in all cases. While the number density of galaxies at $0.5 < z < 1.0$ is similar with that in the local universe, the number density at $2.5 < z < 3.5$ is about an order of magnitude smaller than the local value. Figure 7 and Table 2 show the best-fit Schechter parameters (α, M^*, ϕ^*) estimated with the STY method. The redshift evolution of the overall number density can be seen as the decrease of the normalization of the SMF ϕ^*. ϕ^* decreases down to $\sim$ 50% of that in the local universe at $z \sim 0.75$, $\sim$ 16% at $z \sim 1.25$, $\sim$ 9% at $z \sim 2$, and $\sim$ 3% at $z \sim 3$. Similar evolution of the SMF is also seen in previous studies of general fields (e.g., Fontana et al. 2006; Pérez-González et al. 2008; Marchesini et al. 2009).

Second, we found the mass-dependent evolution of the SMF. The evolution of the number density of low-mass galaxies with $M_{\rm star} \sim 10^9$–10^{10} $M_\odot$ is smaller than that of the massive galaxies with stellar mass $\sim 10^{11}$ $M_\odot$. While the number density of galaxies with $\sim 10^{11}$ $M_\odot$ at $2.5 < z < 3.5$ is smaller by a factor of $\sim$ 20 than the local value, that of the galaxies with $\sim 5 \times 10^9$ $M_\odot$ is smaller by only a factor of $\sim$ 6 at the same redshift. The shape of the SMF at $0.5 < z < 1.0$ is similar with that in the local universe, and it becomes steeper with redshift at $z > 1$. This can be seen in Figure 7 and Table 2 as a steepening of the low-mass slope α with redshift. α decreases with redshift gradually from $\alpha = -1.29 \pm 0.03(\pm 0.04)$ at $0.5 < z < 1.0$ to $\alpha = -1.48 \pm 0.06(\pm 0.07)$ at $1.5 < z < 2.5$ and $\alpha = -1.62 \pm 0.14(\pm 0.06)$ at $2.5 < z < 3.5$. The quoted errors are statistical errors estimated from the maximum likelihood method. The values in parenthesis show the uncertainty due to the different SED models.

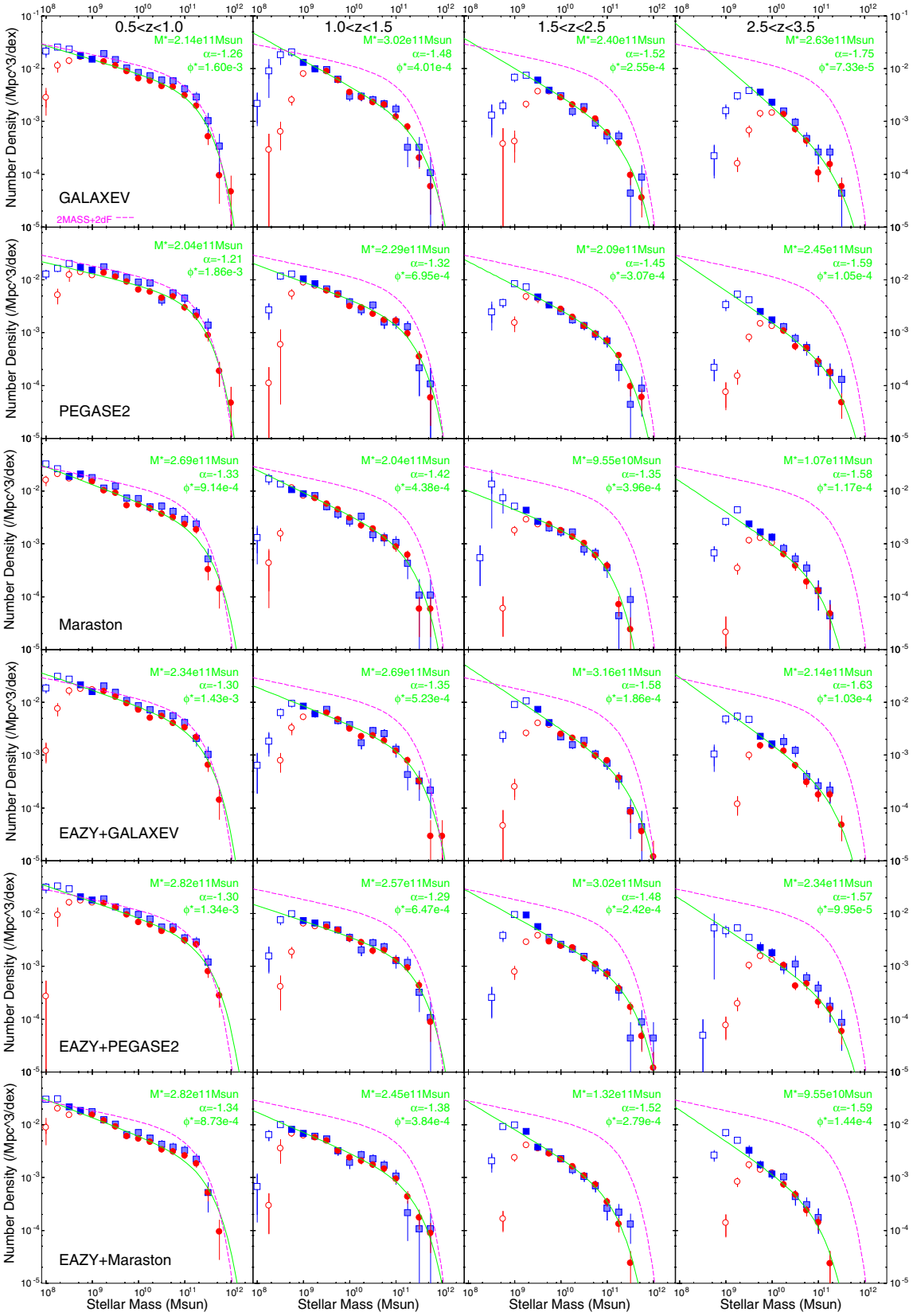

Figure 5. Evolution of the stellar mass function of galaxies in the MODS field. From top to bottom the panels show the results with the different population synthesis models. Circles and squares show the SMF calculated with the $1/V_{\rm max}$ formalism for the wide and deep samples. Open symbols indicate data points located below the limiting stellar mass, where the incompleteness could be significant. Solid symbols show data points above the limiting stellar mass. The results of the deep sample are plotted by shaded symbols at stellar mass where the wide sample is also above the limiting mass. Error bars are based on the Poisson statistics. The solid lines show the results calculated with the STY method for the all (wide and deep) samples. The best-fit Schechter parameters are also shown in each panel. For reference, the local SMF of Cole et al. (2001) is shown as the dashed line.

(A color version of this figure is available in the online journal.)

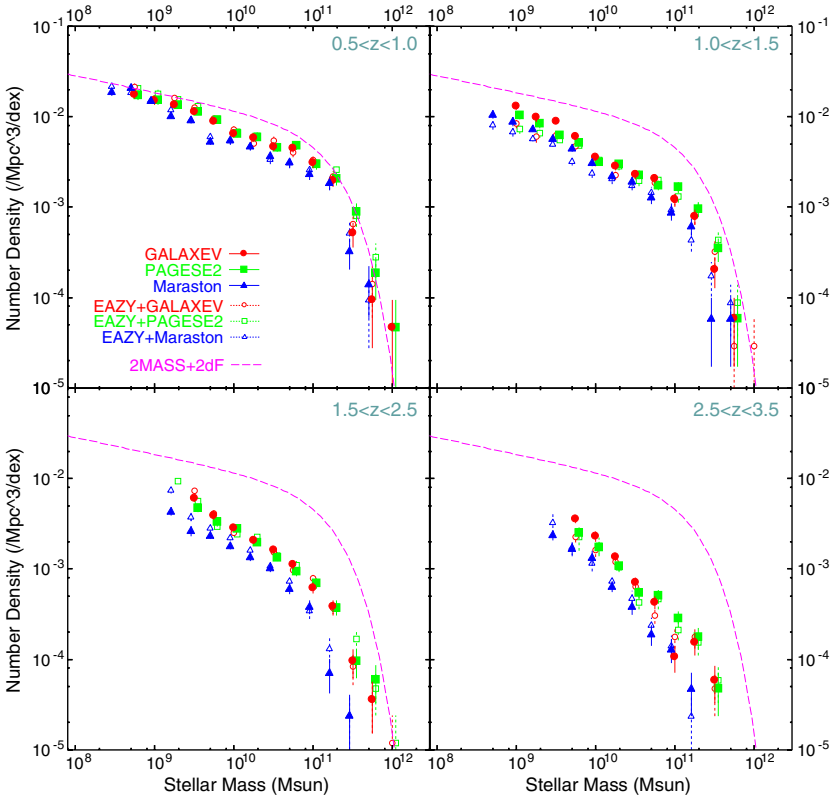

Figure 6. Evolution of stellar mass function for different SED models. For each case, only data points above the limiting stellar mass are plotted. At stellar mass where the wide and deep samples are above the limiting mass, the data points for the wide sample are plotted (the same ones as solid symbols in Figure 5). The dashed line shows the local SMF of Cole et al. (2001).

(A color version of this figure is available in the online journal.)

Table 2
Best-fit Schechter Parameters Obtained with the STY Method

SED Model	Redshift Bin	α	$\log_{10} M^*(M_\odot)$	$\log_{10} \phi^*$ (Mpc^{-3})
GALAXEV	$z = 0.5$–1.0	$-1.26^{+0.03}_{-0.03}$	$11.33^{+0.10}_{-0.07}$	$-2.79^{+0.07}_{-0.08}$
	$z = 1.0$–1.5	$-1.48^{+0.04}_{-0.04}$	$11.48^{+0.16}_{-0.13}$	$-3.40^{+0.13}_{-0.15}$
	$z = 1.5$–2.5	$-1.52^{+0.06}_{-0.06}$	$11.38^{+0.14}_{-0.12}$	$-3.59^{+0.14}_{-0.16}$
	$z = 2.5$–3.5	$-1.75^{+0.15}_{-0.13}$	$11.42^{+0.40}_{-0.24}$	$-4.14^{+0.34}_{-0.51}$
PEGASE2	$z = 0.5$–1.0	$-1.21^{+0.03}_{-0.02}$	$11.31^{+0.07}_{-0.08}$	$-2.73^{+0.07}_{-0.06}$
	$z = 1.0$–1.5	$-1.32^{+0.04}_{-0.04}$	$11.36^{+0.13}_{-0.10}$	$-3.16^{+0.10}_{-0.11}$
	$z = 1.5$–2.5	$-1.45^{+0.06}_{-0.06}$	$11.32^{+0.13}_{-0.10}$	$-3.51^{+0.12}_{-0.15}$
	$z = 2.5$–3.5	$-1.59^{+0.13}_{-0.14}$	$11.39^{+0.32}_{-0.20}$	$-3.98^{+0.26}_{-0.40}$
Maraston	$z = 0.5$–1.0	$-1.33^{+0.02}_{-0.03}$	$11.43^{+0.12}_{-0.10}$	$-3.04^{+0.08}_{-0.10}$
	$z = 1.0$–1.5	$-1.42^{+0.04}_{-0.04}$	$11.31^{+0.14}_{-0.12}$	$-3.36^{+0.12}_{-0.13}$
	$z = 1.5$–2.5	$-1.35^{+0.07}_{-0.08}$	$10.98^{+0.12}_{-0.10}$	$-3.40^{+0.12}_{-0.14}$
	$z = 2.5$–3.5	$-1.58^{+0.19}_{-0.18}$	$11.03^{+0.31}_{-0.21}$	$-3.93^{+0.30}_{-0.43}$
EAZY + GALAXEV	$z = 0.5$–1.0	$-1.30^{+0.03}_{-0.03}$	$11.37^{+0.10}_{-0.08}$	$-2.84^{+0.07}_{-0.08}$
	$z = 1.0$–1.5	$-1.35^{+0.04}_{-0.05}$	$11.43^{+0.15}_{-0.11}$	$-3.28^{+0.11}_{-0.14}$
	$z = 1.5$–2.5	$-1.58^{+0.05}_{-0.06}$	$11.50^{+0.18}_{-0.13}$	$-3.73^{+0.15}_{-0.20}$
	$z = 2.5$–3.5	$-1.63^{+0.14}_{-0.15}$	$11.33^{+0.32}_{-0.20}$	$-3.99^{+0.28}_{-0.42}$
EAZY + PEGASE2	$z = 0.5$–1.0	$-1.30^{+0.03}_{-0.02}$	$11.45^{+0.09}_{-0.09}$	$-2.87^{+0.08}_{-0.07}$
	$z = 1.0$–1.5	$-1.29^{+0.04}_{-0.05}$	$11.41^{+0.13}_{-0.10}$	$-3.19^{+0.09}_{-0.13}$
	$z = 1.5$–2.5	$-1.48^{+0.04}_{-0.05}$	$11.48^{+0.14}_{-0.12}$	$-3.62^{+0.14}_{-0.15}$
	$z = 2.5$–3.5	$-1.57^{+0.15}_{-0.14}$	$11.37^{+0.32}_{-0.22}$	$-4.00^{+0.28}_{-0.39}$
EAZY + Maraston	$z = 0.5$–1.0	$-1.34^{+0.02}_{-0.03}$	$11.45^{+0.13}_{-0.09}$	$-3.06^{+0.07}_{-0.11}$
	$z = 1.0$–1.5	$-1.38^{+0.04}_{-0.04}$	$11.39^{+0.17}_{-0.12}$	$-3.42^{+0.12}_{-0.14}$
	$z = 1.5$–2.5	$-1.52^{+0.06}_{-0.07}$	$11.12^{+0.14}_{-0.11}$	$-3.55^{+0.13}_{-0.17}$
	$z = 2.5$–3.5	$-1.59^{+0.18}_{-0.17}$	$10.98^{+0.27}_{-0.20}$	$-3.84^{+0.28}_{-0.38}$

The uncertainty of the Schechter parameters becomes larger with redshift, especially at $2.5 < z < 3.5$, because of the larger limiting mass at higher redshift and of the small number of galaxies even at relatively high mass due to the evolution of the

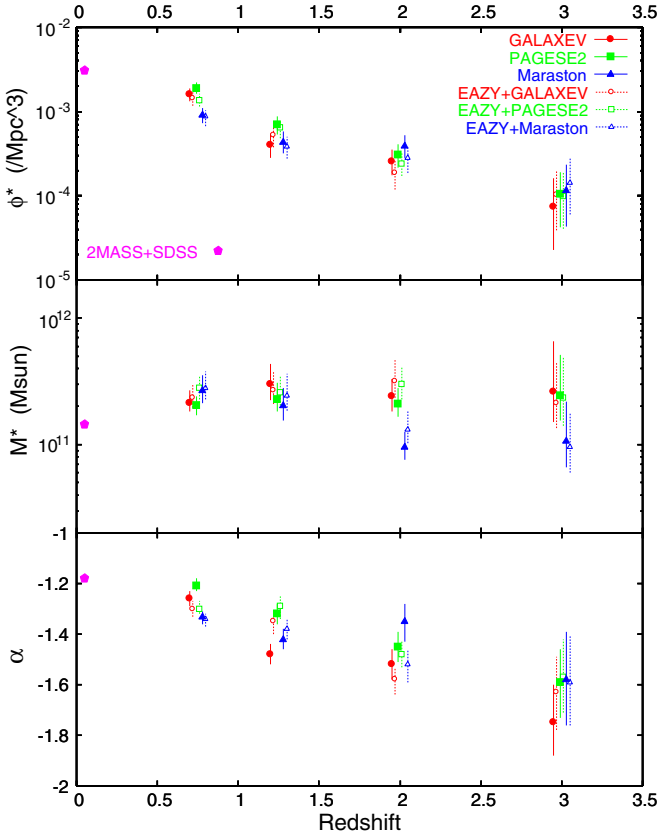

Figure 7. Best-fit Schechter parameters as a function of redshift. Different symbols represent the results with different population synthesis models. Data points for different SED models are plotted with small horizontal offsets for clarity. Those of the local SMFs of Cole et al. (2001) are also shown for reference.

(A color version of this figure is available in the online journal.)

overall number density mentioned above. Nonetheless, since the uncertainty at $z < 2.5$ is rather small by virtue of our deep and wide NIR data, the evolution of the low-mass slope of the SMF between $0 \lesssim z \lesssim 3$ is found to be significant. Figure 8 shows the best-fit Schechter parameters and their uncertainty for the different SED models in the M^*–α plane, which represents the evolution of the shape of the SMF. In all cases, the evolution of α is significant, although there is degeneracy between M^* and α especially at $2.5 < z < 3.5$, where we can reach only to the relatively high stellar mass.

On the other hand, the characteristic mass M^* shows no significant evolution except for the results with the Maraston model. The M^* values at $0.5 < z < 3.5$ are similar with or slightly larger than those in the local universe. No significant evolution for M^* is also seen in previous studies (Fontana et al. 2006; Pozzetti et al. 2007; Marchesini et al. 2009). For the Maraston model, M^* becomes smaller by a factor of $\sim$ 2–2.5 at $z > 1.5$. As in the above discussion of the overall number density, this can be explained by the systematically lower stellar M/L ratio of the Maraston model because the same result is also seen when the same photometric redshifts (EAZY) are used. While passively evolving galaxies dominate the massive end ($\gtrsim 10^{11}\ M_\odot$) of the SMF at $z \lesssim 1$ (e.g., Juneau et al. 2005; Borch et al. 2006; Vergani et al. 2008; Ilbert et al. 2009), many massive star-forming (i.e., relatively young) galaxies have been found at $z \sim 2$ (e.g., Daddi et al. 2007; Papovich et al. 2006; Borys et al. 2005; Shapley et al. 2004). It is possible that TP-AGB stars contribute to the SED of massive galaxies significantly only at $z > 1.5$. Therefore, the Maraston model would give systematically lower stellar mass for these massive galaxies.

3.5. Possible Biases for the Evolution of the Low-mass Slope

Here we investigate possible biases for the results in the previous subsection, in particular, systematic effects which could cause the steepening of the low-mass slope at high redshift.

The larger limiting mass at higher redshift causes the degeneracy between M^* and α as mentioned in the previous section. Since low-mass galaxies near the limiting mass tend to be faint in each band, the photometric errors are larger, which results in the large uncertainty in their photometric redshift. The large errors of the photometric redshifts of faint objects might lead to the systematic increase of the low-mass galaxies at high redshift because the redshift distribution of the K-selected sample has a peak around $z \sim 1$ and a tail to higher redshift. In order to evaluate the effect on the low-mass slope, we performed a Monte Carlo simulation, assuming no evolution of the shape of the SMF (i.e., constant M^* and α). At first, we constructed mock catalogs with the observed M^* and α at $0.5 < z < 1.0$. For the normalization of the SMF, we assumed ϕ^* evolving as $\phi^*(z) \propto (1+z)^{-2}$ so that the redshift distribution of the mock sample is consistent with our observation. Even if we assume $\phi^*(z) \propto (1+z)^{-1}$ or $\phi^*(z) \propto (1+z)^{-3}$, the results shown in the following do not change significantly. Stellar mass and redshift of mock objects were randomly selected from the ranges of $10^8\ M_\odot < M_{\rm star} < 10^{12}\ M_\odot$ and $0 < z < 6$, using the probability distribution estimated from the assumed SMF and the corresponding comoving volume of our survey at each redshift. For each mock object, we randomly extract an object from the observed sample with similar mass and redshift (allowing duplicate) and adopted its observed multiband photometry. The observed multiband photometry was extracted from the catalog that contains all sources detected on the K-band image (including $K > 23$ or $K > 24$ objects) in order to take into account the scattering of objects fainter than the magnitude limits. Then we added random offsets to the multiband photometry according to the measured photometric errors, and adopted the mock object if the resulting K-band magnitude of the object was brighter than the magnitude limits ($K < 23$ for the wide sample and $K < 24$ for the deep sample). We repeated this procedure and made the mock catalogs with the same sample sizes as the observed wide and deep samples. The same SED-fitting procedure as for the observed one was performed in order to estimate the photometric redshift and stellar mass of the mock objects. For objects with spectroscopic identification, redshifts are fixed to the spectroscopic values. We performed 200 simulations and calculated the best-fit Schechter parameters in each simulation with the STY method.

Figure 9 shows the results of the simulation in the case with GALAXEV (the results for the other models are similar). A relatively large scatter of α is seen in the highest redshift bin, which probably reflects the large degeneracy between M^* and α due to the large limiting mass. Furthermore, the simulated α distributes around a systematically steeper (by $\sim$ 0.1–0.15) value than the assumed one at $2.5 < z < 3.5$, while the simulated values tend to be slightly flatter (by $\sim$ 0.1) in lower redshift bins. However, since the observed evolution of α is much stronger than the systematic effects in Figure 9, the observed steepening of the low-mass slope at high redshift is significant, especially at $1 < z < 2.5$.

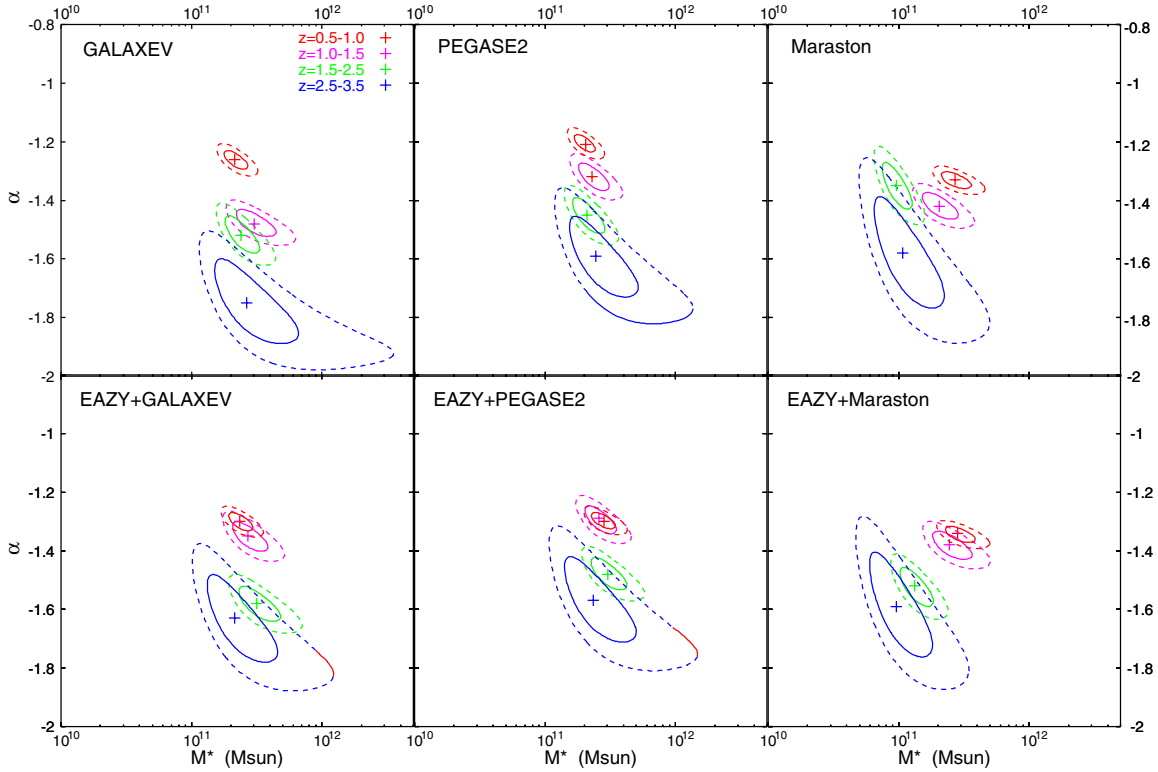

Figure 8. Evolution of the Schechter parameters in M^*–α plane for the different SED models. Crosses show the best-fit values determined with the STY method. 1σ (solid) and 2σ (dashed) error contours are also shown.

In the simulation, the random offsets added to the multiband photometry and the recalculation of the photometric redshift include the effect of the catastrophic failure. We extracted the mock objects whose photometric redshift was changed catastrophically ($\delta z/(1+z) > 0.5$) by the random offsets and checked the effect of these objects on the resulting SMF. Figure 10 shows the fractional increase and decrease of the number of galaxies due to the catastrophic failure of the photometric redshift as a function of stellar mass in each redshift bin. At $0.5 < z < 1.5$, there is ∼10%–20% decrease near the limiting stellar mass, while there is only negligible effect of the catastrophic failure at $M_{\rm star} \gtrsim 10^{10}\ M_\odot$. Most contamination from $z < 0.5$ or $z > 1.5$ occurs only at the stellar mass lower than limiting mass and it is not plotted in the figure. About 10%–20% decrease near the limiting stellar mass might cause a slightly flatter low-mass slope seen in Figure 9, but the effect is relatively small (∼0.1 dex decrease in the number density). At $z > 1.5$, the effect of the catastrophic failure is similar or even smaller than that at low redshift. Furthermore, the contamination from lower redshift and the dropout from the redshift bin tend to be canceled out with each other, which results in the negligible effect on the SMF.

In Figure 11, we also show the results of the same simulation on the α–ϕ^* plane to investigate the effect on the normalization. The systematic effect on the normalization of the SMF due to the photometric redshift errors seems to be relatively small, although the degeneracy between the parameters makes direct comparison difficult.

Next, we discuss a possibility of the over-deblending of faint objects with relatively low S/N ratio near the detection limit. Although the K band, where we performed the source detection, corresponds to the rest-frame B band even at $z = 3.5$, the morphological K correction could enhance the over-deblending at high redshift because galaxies tend to show the patchy appearance in shorter wavelengths due to the dominance of young stars and the dust extinction (e.g., Kuchinski et al. 2001; Rawat et al. 2009). Figure 12 shows the fraction of the objects with the deblending flag by SExtractor as a function of stellar mass in each redshift bin for the wide and deep samples. We cannot see the mass nor redshift dependence of the fraction of the deblended objects. We conclude that the effect of deblending does not cause the evolution of the low-mass slope.

Finally, we estimated the stellar mass of galaxies in the highest redshift bin with the GALAXEV templates with two-component (old and young) SFHs. If the old stellar population is hidden by recent star formation, the stellar mass could be underestimated especially for relatively blue low-mass galaxies at high redshift, where the S/N ratio tends to be low (e.g., Papovich et al. 2001; Drory et al. 2005). We used the exponentially decaying star formation models (young component) with an old population component. For the young population, free parameters are stellar age, star formation timescale τ, color excess, metallicity (same as for one-component SFH). For the old component, we limited the star formation timescale and stellar age to shorter and older values than the young population, respectively, and assumed no dust extinction. Figure 13 shows the comparison of the stellar masses estimated with one- and two-component models for galaxies at $2.5 < z < 3.5$. No significant systematic difference of the stellar mass can be seen. The scatter is consistent with the uncertainty of the stellar mass of these galaxies shown in Figure 2, although the stellar mass with the two-component model is slightly larger for a small fraction of galaxies at low-mass end. The long wavelength data with *Spitzer*/IRAC, which sample the rest-frame NIR region even at high redshift, could make the systematic uncertainty relatively small (Fontana et al. 2006; Elsner et al. 2008).

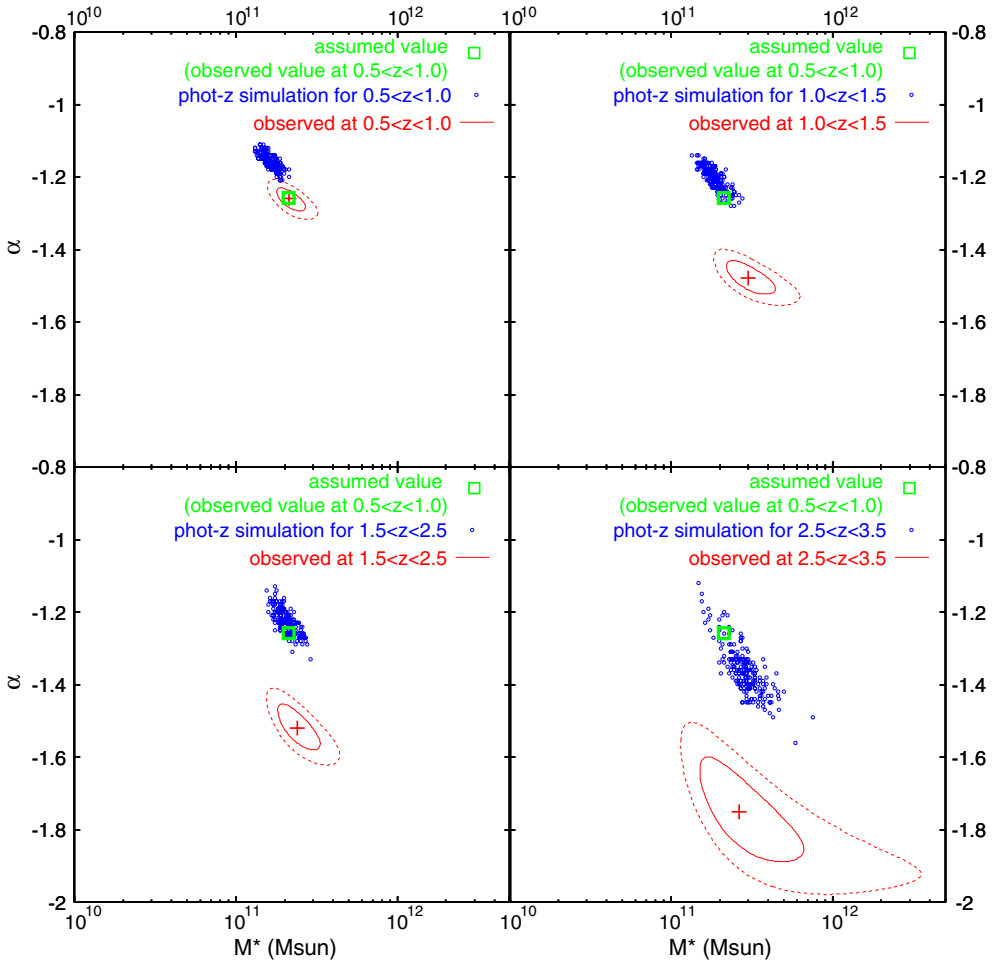

Figure 9. Monte Carlo simulation for the effects of photometric redshift uncertainty on the shape (M^* and α) of the stellar mass function with the GALAXEV model. The large square in each redshift bin shows the observed values at $0.5 < z < 1.0$, and these are assumed not to evolve with redshift in the simulation. Small circles show the results of 200 simulations (see the text for details). Observed M^*–α values (cross) and 1σ (solid) and 2σ (dashed) error contours are also shown for each redshift bin.

(A color version of this figure is available in the online journal.)

4. DISCUSSION

We have studied the evolution of the SMF of galaxies back to $z \sim 3$ using the NIR Subaru/MOIRCS data obtained in the MODS and the publicly available multiwavelength GOODS data. Our deep and wide NIR data allowed us to estimate the number density of galaxies down to low stellar mass ($\sim 10^9$–$10^{10}\ M_\odot$) even at $z \sim 2$–3 with high accuracy. Main results in the previous section are (1) the decrease of the overall number density of galaxies with redshift and (2) the steepening of the low-mass slope of the SMF at high redshift. In this section, we first compare the results with previous studies and then discuss the implications for galaxy formation and evolution in the following.

4.1. Comparison with Previous Studies

In this subsection, we compare our results in the MODS field with those in other general fields.

Figure 14 shows a comparison of the integrated stellar mass density as a function of redshift. We calculated the stellar mass density by integrating the best-fit Schechter function over 10^8–$10^{13} M_\odot$ in each redshift bin. Different symbols represent the results with the different SED models. Compilations of Wilkins et al. (2008) and Marchesini et al. (2009) are also plotted. All data points are the results with the Salpeter IMF. The stellar mass density in the MODS field decreases with redshift as seen in other previous studies. When compared with those in the local universe, the stellar mass density is ∼53%–72% of the local value at $0.5 < z < 1.0$, ∼22%–34% at $1.0 < z < 1.5$, ∼8%–18% at $1.5 < z < 2.5$, and ∼4%–9% at $2.5 < z < 3.5$. For the GALAXEV model, which is widely used in other previous studies (e.g., Drory et al. 2005; Fontana et al. 2006; Pozzetti et al. 2007; Elsner et al. 2008; Marchesini et al. 2009), our results are consistent with those of previous studies at each redshift (Figure 14). A slightly large value at $0.5 < z < 1.0$ is probably due to the large-scale structures around the HDF-N mentioned above. As discussed in Section 3.4, the Maraston model gives systematically lower stellar mass density, which is about three-quarters of those with the other two models (GALAXEV and PEGASE2) at $0.5 < z < 1.0$, about two-thirds at $1.0 < z < 1.5$ and about a half at $z > 1.5$.

In Figure 15, we compare the SMF of galaxies in the MODS field with those in other studies. For simplicity, we plotted the result with the GALAXEV model. At the massive end ($\gtrsim 10^{11}\ M_\odot$), our result is consistent with those in other general fields, although the uncertainty of our data and the variance among the different surveys are relatively large because of the

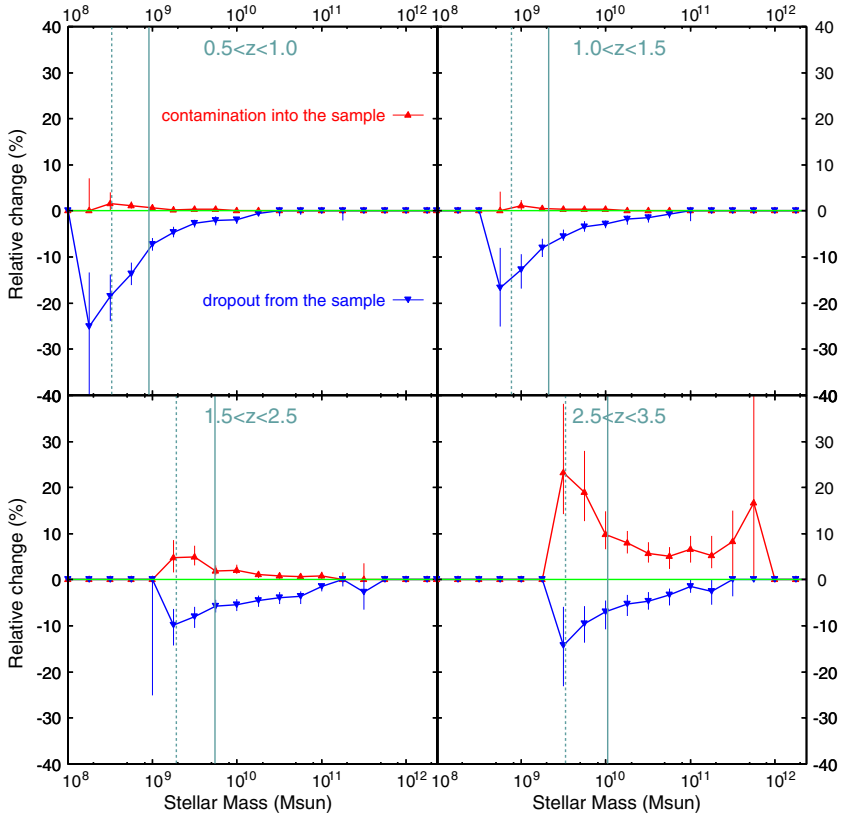

Figure 10. Effect of the catastrophic failure of the photometric redshift on the SMF in the Monte Carlo simulation. Upward and downward triangles show the fractional increase and decrease of the number of galaxies as a function of stellar mass in each redshift bin due to the objects whose photometric redshift was changed catastrophically ($\delta z/(1+z) > 0.5$) by the random offsets of the multiband photometry. Upward (downward) triangles represent the fraction of the objects which enter into (drop out from) the redshift bin due to the catastrophic failure. Data points and error bars represent the median value and 68 percentile interval of the 200 simulations. Vertical lines show the limiting stellar mass for the wide (solid) and deep (dashed) samples.

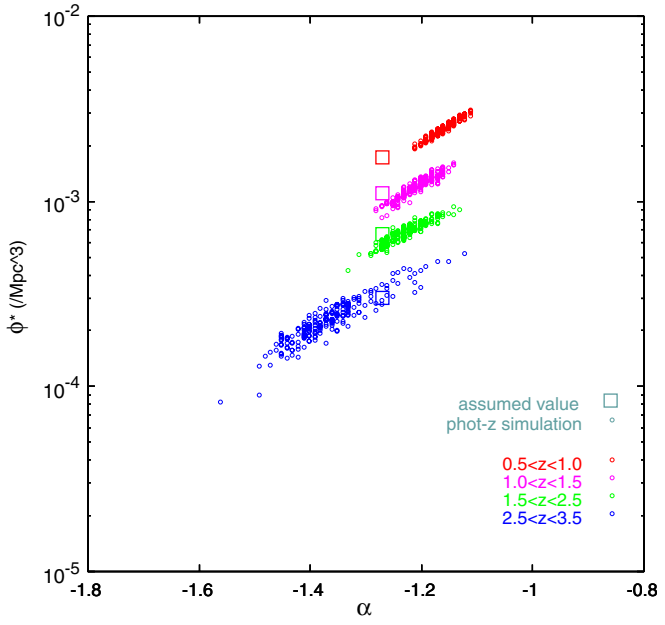

Figure 11. Effect of photometric redshift uncertainty on the normalization (ϕ^*) of stellar mass function. Large squares and small circles are the same as those in Figure 9, but different colors represent different redshift bins. The normalization is assumed to evolve with redshift as $\phi^*(z) \propto (1+z)^{-2}$ (see the text).

small number of observed massive galaxies and probably their strong clustering (e.g., van Dokkum et al. 2006; Conselice et al. 2007; Stringer et al. 2009). The agreement of the SMF at the massive end is consistent with the comparison of the integrated stellar mass density because galaxies around M^* ($\sim 10^{11}\ M_\odot$) dominate the stellar mass density (e.g., Gwyn & Hartwick 2005, see also next subsection). No significant evolution of M^* seen in the MODS field at $0.5 < z < 3.5$ is also consistent with results of previous studies (Fontana et al. 2006; Bertone et al. 2007; Pozzetti et al. 2007; Elsner et al. 2008; Pérez-González et al. 2008; Marchesini et al. 2009).

On the other hand, at the lower mass of the SMF, there is some variance in different fields including the MODS field in spite of the relatively small statistical errors. In addition to the differences in the normalization, which are similar offsets with those at the massive end, there is differences in the low-mass slope especially at high redshift. One possible reason for this is the different depths of the surveys and therefore the different limiting stellar masses. The SMF in the MODS field shows a slight upturn around $\sim 10^{10}\ M_\odot$ and a steeper slope at $< 10^{10}\ M_\odot$, although this is marginal in the highest redshift bin. This indication can be seen in the results with all SED models (Figure 5) and does not depend on the systematic error of the photometric redshift and stellar M/L ratio. Similar upturns in the SMF are also seen in field galaxies in the local universe (Baldry et al. 2008) and at intermediate and high redshift (Fontana et al. 2006; Pozzetti et al. 2007; Elsner et al. 2008). Therefore, the relatively shallow survey with the limiting stellar mass larger than $\sim 10^{10}\ M_\odot$ could miss the upturn and result in the systematically flatter low-mass slope even if the completeness to the limit is sufficiently high or the incompleteness correction is properly done. For example, the SMFs from the different surveys show consistent low-mass slopes in the $0.5 < z < 1.0$ bin in Figure 15, where all the surveys reach below $10^{10}\ M_\odot$.

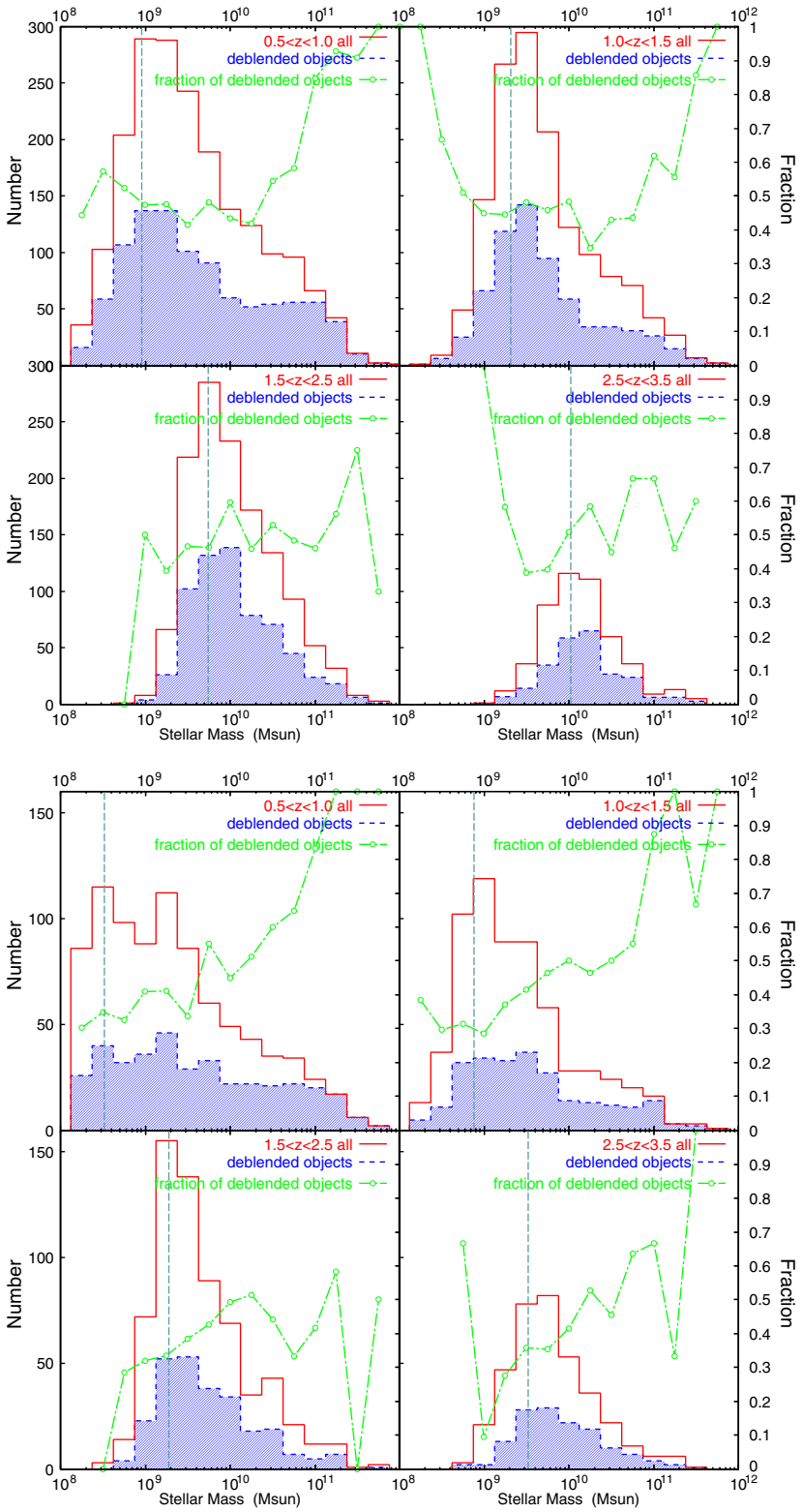

Figure 12. Fraction of deblended objects as a function of stellar mass in each redshift bin for the wide (top) and deep (bottom) samples. The solid line shows all *K*-selected galaxies in each redshift bin and the shaded histogram represents deblended objects. The dashed-dot line shows the fraction of the deblended objects. Vertical long-dashed line shows the limiting stellar mass. The results with the GALAXEV model are shown.

(A color version of this figure is available in the online journal.)

At $1.0 < z < 1.5$, several surveys reach only to $\sim 10^{10}\ M_{\odot}$. While the slope at 10^{10}–$10^{11}\ M_{\odot}$ is similar with those in other surveys, the SMF in the MODS field shows the steeper slope at 10^{9}–$10^{10}\ M_{\odot}$ than that at larger stellar mass. This could be the case in the higher redshift bins.

At $z > 1.5$, on the other hand, Elsner et al. (2008) and Marchesini et al. (2009) reach below $10^{10}\ M_{\odot}$ and show the flatter low-mass slopes than those in the present study. In Elsner et al. (2008), the low-mass slope is fixed to the weighted mean value $\alpha \sim -1.36$, which is constrained mainly by galaxies at

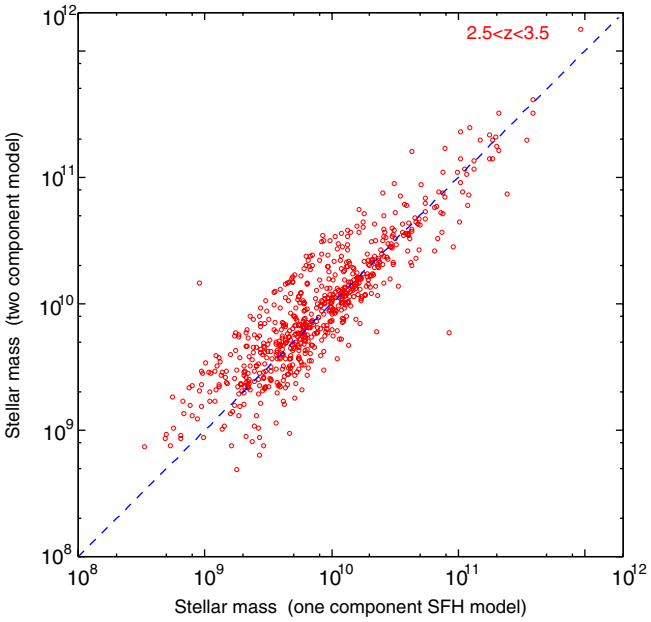

Figure 13. Comparison between the stellar masses estimated with the one-component SFH model and two-component (old and young) model for galaxies at $2.5 < z < 3.5$. The result with the GALAXEV model is shown.

relatively low redshift ($z \lesssim 1$, their Figure 7). Marchesini et al. (2009) discussed the effects of various random and systematic uncertainties on the estimate of the Schechter parameters of the SMF and suggested that the uncertainty of the low-mass slope in their analysis is relatively large especially at high redshift due to the statistical error and the systematic errors of the different SED models. The difference in the low-mass slope between Marchesini et al. (2009) and the present study could be attributed to field-to-field variance. In the local universe, several studies suggest that the shape of the SMF depends on the environment of galaxies (Balogh et al. 2001; Baldry et al. 2006; Baldry et al. 2008), and this could be the case at higher redshift (e.g., Scodeggio et al. 2009). In Marchesini et al. (2009), the low-mass slope at high redshift is constrained mainly by the FIRES data, whose survey area is about a fifth of our study. If the shape of the SMF depends on the environment even at high redshift, the low-mass slope estimated from the small area surveys could be affected by the field-to-field variance. A larger area survey with a similar or fainter limiting magnitude in the NIR wavelength is needed to conclude whether there exists the field-to-field variance of the shape of the SMF at $z \sim 2$–3 or not.

4.2. Mass-dependent Evolution of Galaxies

The decrease of the overall number density and the steepening of the low-mass slope with redshift seen in the evolution of the SMF of galaxies in the MODS field suggest the possibility of the mass-dependent number density evolution. Figure 16 shows the evolution of the number density of galaxies in different stellar mass ranges for the different SED models. Relatively low-mass galaxies with the stellar mass of $10^{9.5}$–$10^{10.5}$ $M_\odot$ tend to show a weaker evolution of the number density especially at $z \gtrsim 1.5$ than M^* ($\sim 10^{11}$ $M_\odot$) galaxies, although the trend is relatively marginal in the results with the GALAXEV/PEGASE2 models. The relative number density of low-mass galaxies had been larger at high redshift than that in the local universe. In other words, the number density of galaxies around M^* might have more rapidly increased at $z \gtrsim 1.5$ than that of low-mass galaxies. On the other hand, several studies based on wide area but shallow surveys suggest that for $M_{\rm star} > 10^{11}$ $M_\odot$, more massive (e.g., $\gtrsim 10^{11.5}$–10^{12} $M_\odot$) galaxies show weaker evolution in the number density at $z \gtrsim 1.5$ (Berta et al. 2007; Pérez-González et al. 2008). Although the survey volume of the present study is not large enough to constrain strongly the number density of very massive galaxies with $10^{11.5}$–10^{12} $M_\odot$, galaxies around 10^{11} $M_\odot$ might have been formed effectively at $1 \lesssim z \lesssim 3$ compared with higher and lower mass galaxies (e.g., Fontana et al. 2004; Franceschini et al. 2006).

Figure 17 shows the contribution of galaxies in different stellar mass ranges to the cosmic stellar mass density. While

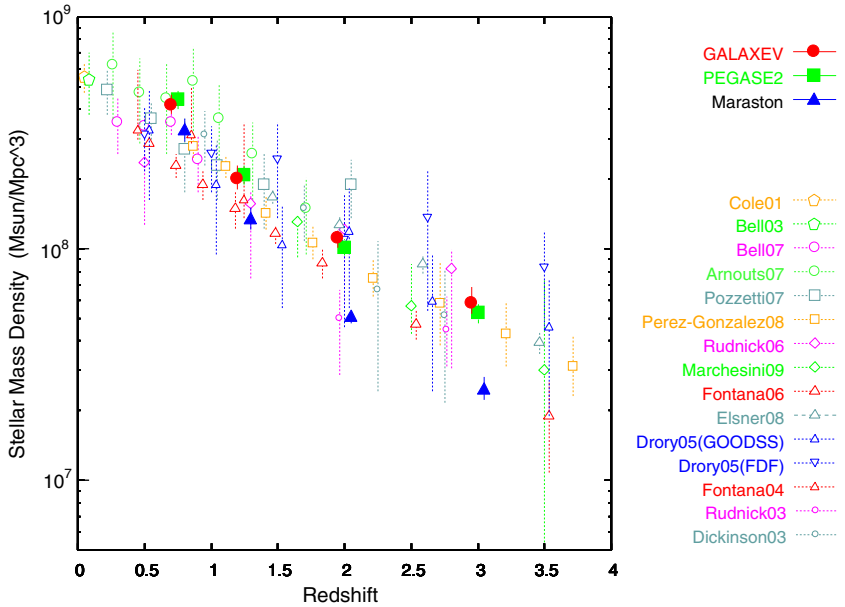

Figure 14. Evolution of the stellar mass density (integrated over 10^8 $M_\odot$ < $M_{\rm star}$ < 10^{13} $M_\odot$) as a function of redshift for the different SED models (solid symbols). Error bars are based on the Poisson statistics. Open symbols show results from previous surveys (compilations from Wilkins et al. 2008 and Marchesini et al. 2009). Some data points are shifted horizontally for clarity.

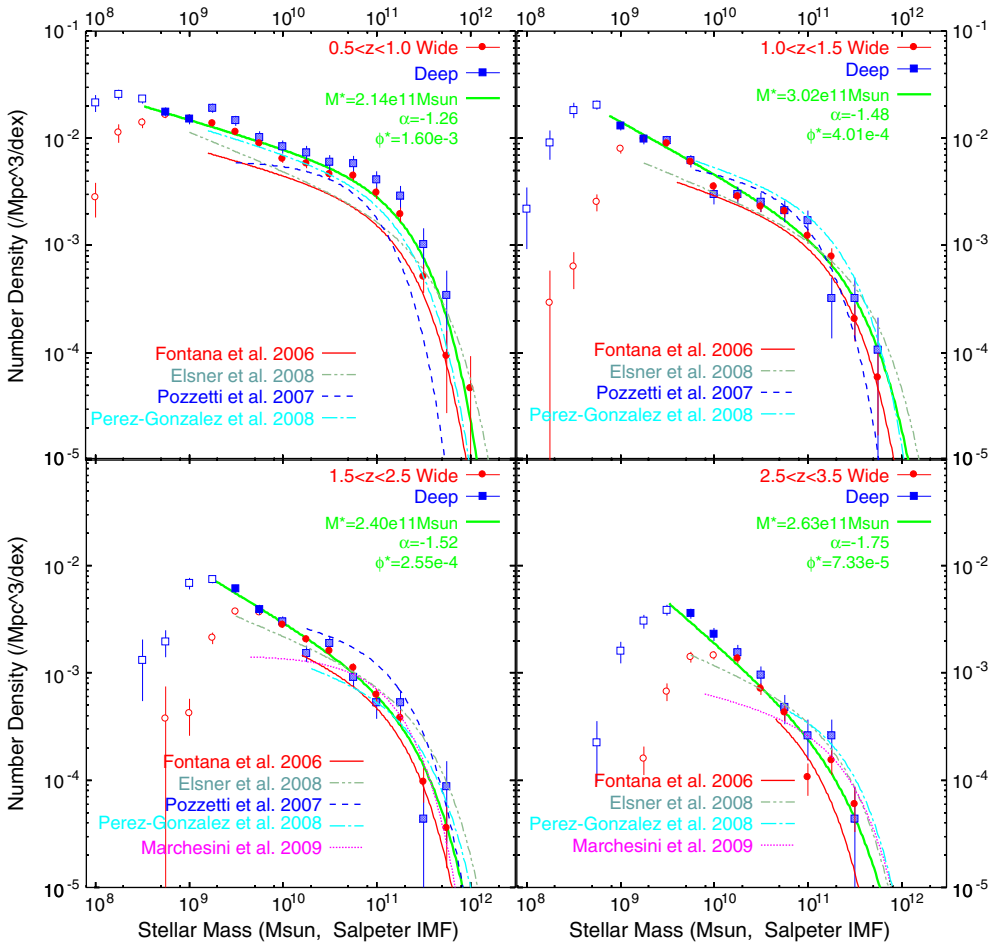

Figure 15. Comparison between stellar mass functions in this study and other surveys. The GALAXEV model is used for the direct comparison with previous studies. Circles, squares, and solid line are the same as those in Figure 5. For other deep surveys, the best-fit Schechter functions from the literature (Fontana et al. 2006; Elsner et al. 2008; Pozzetti et al. 2007; Pérez-González et al. 2008; Marchesini et al. 2009) are plotted over the observed mass range.

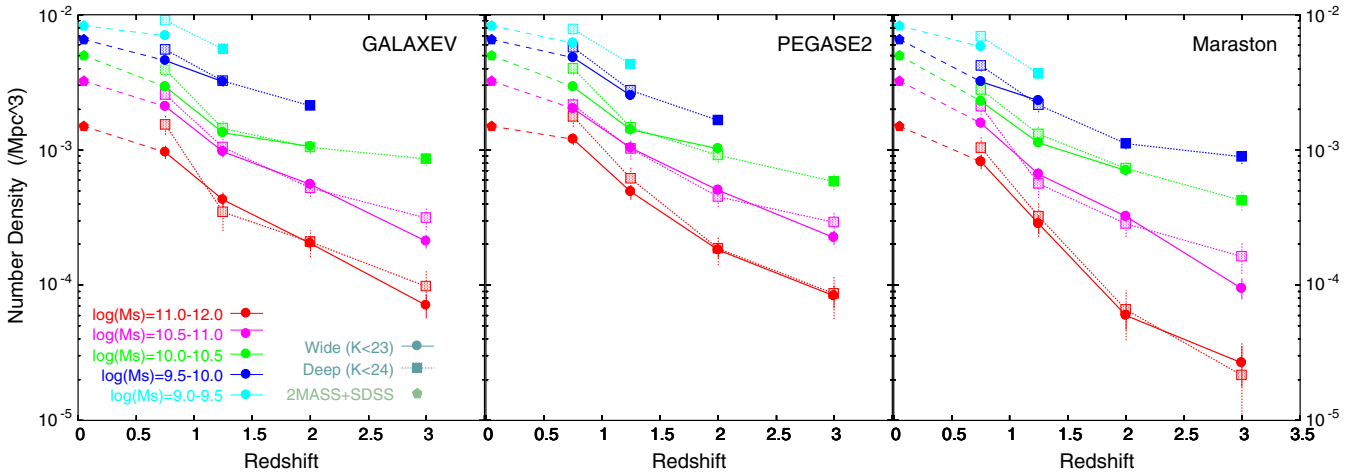

Figure 16. Evolution of the number density of galaxies in different stellar mass ranges. Three panels represent the results with the different SED models. Circles and squares show the wide and deep samples, respectively. Different colors of the symbols represent different ranges of the stellar mass of galaxies. Only stellar mass ranges which are above the limiting stellar mass in Figure 4 at each redshift are shown.

the stellar mass density is dominated by massive galaxies with $M_{\rm star} > 10^{10.5}\,M_{\odot}$ in the local universe, the contribution of lower mass galaxies increases with redshift and is significant at $z \sim 3$. Reddy & Steidel (2009) reported a relatively steep faint-end slope ($\alpha \sim -1.7$) of the luminosity function for Lyman Break Galaxies (LBGs) at $1.9 < z < 3.4$. They estimated the stellar mass of faint LBGs with the log-linear relation between SFR and stellar mass derived in Sawicki et al. (2007), and suggested that those faint LBGs, which typically have $M_{\rm star} \lesssim 10^{10}\,M_{\odot}$ (Figure 12 in Reddy & Steidel 2009), show a significant contribution to the total stellar mass density. Since most low-mass galaxies at $z \sim 2$–3 have rather blue rest-frame colors

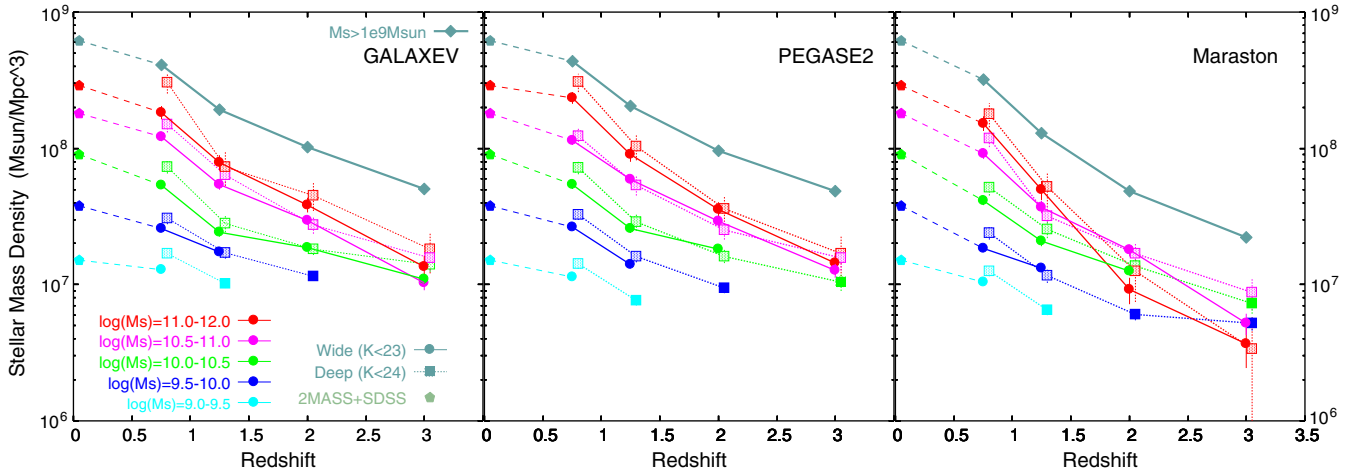

Figure 17. Contributions of different stellar mass ranges to the total stellar mass density as a function of redshift. Symbols are the same as in Figure 16. Diamonds show the stellar mass density integrated over $10^9\ M_\odot < M_{\rm star} < 10^{12}\ M_\odot$ at each redshift.
(A color version of this figure is available in the online journal.)

(typically rest $U-V \lesssim 0$, Figure 3; Kajisawa & Yamada 2005; Kajisawa & Yamada 2006) and satisfy the LBG criteria (Labbé et al. 2005), the steep low-mass slope of the SMF at high redshift in our study seems to be consistent with the result in Reddy & Steidel (2009). Note that the integrated stellar mass density in the MODS field is consistent with those of other previous studies as mentioned in the previous subsection, but about a half of the estimate in Reddy & Steidel (2009). Then, although the contribution of low-mass galaxies to the total stellar mass density in the MODS field is larger than those estimated in previous studies, the stellar mass density is still smaller than that expected from the evolution of the cosmic SFR density (e.g., Wilkins et al. 2008; Reddy & Steidel 2009).

4.3. The Origin of the Evolution of the Low-mass Slope

What is the origin of the evolution of the low-mass slope? In hierarchical structure formation scenarios, low-mass objects continue to grow by merging over cosmic time and result in more massive objects at later epochs. Therefore, one can expect the steeper low-mass slope at the higher redshift (e.g., Khochfar et al. 2007; Ryan et al. 2007). Figure 18 compares the observed SMF in the MODS field with the predictions of the publicly available semi-analytic models by Bower et al. (2006) and Bertone et al. (2007). These two models are based on the Millennium Simulation of the growth of dark matter structure in a Λcold dark matter cosmology (Springel et al. 2005) but are made by the different procedures in many aspects such as, e.g., the construction of halo merger trees, the implementation of the star formation, the feedback by supernova explosions and active galactic nuclei activities. We convolved these model predictions with the Gaussian representing the uncertainty of the stellar mass estimate shown in Figure 2. The median value in Figure 2 is chosen as the width of the Gaussian depending on galaxy's stellar mass and redshift. In the models, the low-mass slope similarly steepens with redshift in Figure 18. However, it should be noted that there are discrepancies between the observation and the models in the detailed shape of the SMF and that the evolution of the overall number density of model galaxies is significantly weaker (i.e., larger number density at high redshift) than that of the present observation especially at low mass as in previous studies (e.g., Fontana et al. 2006; Kitzbichler & White 2007; Bertone et al. 2007). On the other hand, several studies found that semi-analytic models tend to predict the smaller number density of galaxies at the massive end ($M_{\rm star} \gtrsim 10^{11.5}$–$10^{11.75}\ M_\odot$) than observations (e.g., Conselice et al. 2007; Bertone et al. 2007). A similar indication is also seen in Figure 18, although our data cannot strongly constrain the number density of these very massive galaxies.

Since the stellar mass of a galaxy is generally dominated by long-lived low-mass stars, it can be generally considered as the integral of the past SFR and expected to increase monotonically with time. Therefore, for example, only suppression of star formation in low-mass galaxies cannot cause the flattening of the low-mass slope of the SMF with time, while it could lead to the evolution of the faint-end slope of the rest-frame UV luminosity function, which directly reflects the SFR, as discussed in Reddy & Steidel (2009). On the other hand, the stellar mass growth by star formation activities in each galaxy could change the slope of the SMF. There are several observational studies that suggest that low-mass galaxies have higher SFR relative to their stellar mass (i.e., SFR/$M_{\rm star}$, specific SFR) than massive galaxies even at $z \sim 2$–3 (e.g., Feulner et al. 2005; Papovich et al. 2006; Reddy et al. 2006b, see also Santini et al. 2009). These results for the mass dependence of SFR/$M_{\rm star}$ suggest that the expected growth rate of stellar mass by star formation activities in a galaxy is higher in lower mass galaxies. If we assume the observed trends of the low-mass slope and mass dependence of SFR/$M_{\rm star}$ continue down to lower mass, a net increase of the number of galaxies in a mass bin due to star formation activities (inflow from lower mass bins − outflow into higher mass bins) is expected to be larger at lower stellar mass, which leads to the steepening of the low-mass slope with time, i.e., opposite to that seen in Figures 5 and 6. For example, Drory & Alvarez (2008) calculated the expected change of the SMF due to star formation only from the average SFR at each stellar mass of galaxies in the FORS Deep Field (Feulner et al. 2005) and showed that the number density of lower mass galaxies is expected to increase more rapidly with time especially at $z \lesssim 3$. By subtracting the expected contribution due to star formation from the observed redshift evolution of the SMF, Drory & Alvarez (2008) evaluated the effect of the hierarchical merging on the evolution of the SMF (i.e., destroying small galaxies and building more massive ones). In their analysis, at $M_{\rm star} \lesssim 10^{10}\ M_\odot$, lower mass galaxies

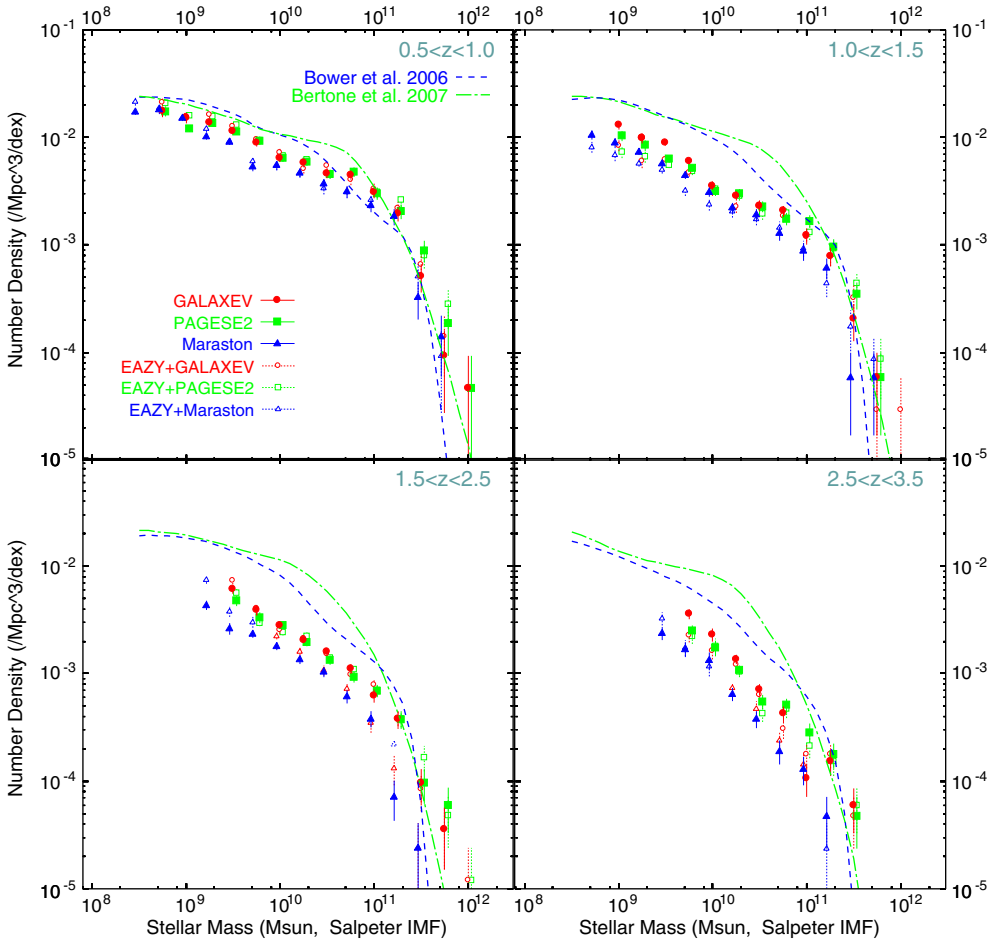

Figure 18. Comparison of the observed stellar mass function with the predictions by the semi-analytic models. Short-dashed line refers to the Bower et al. (2006) model and dashed-dot line represents the Bertone et al. (2007) model. Circles, squares and triangles are the same as in Figure 6.

(A color version of this figure is available in the online journal.)

tend to be consumed in mergers at higher rate to counterbalance the effect of the mass-dependent SFR. Since no evolution of the low-mass end slope is assumed in Drory & Alvarez (2008), the steepening with redshift indicates the effect of merging larger than that estimated in Drory & Alvarez (2008). Therefore, the evolution of the SMF of galaxies in the MODS field suggests that the hierarchical merging process was important for the stellar mass assembly of these low-mass galaxies at $z \sim 1$–3, when the cosmic stellar mass density had been increasing rapidly. The relatively high fraction of peculiar/irregular morphology in low-mass galaxies at $z > 1$ in the NIR wavelength (Kajisawa & Yamada 2005; Conselice et al. 2005) might also imply intense merging activity of these galaxies.

In this context, the fact that low-mass galaxies tend to have relatively younger stellar age and higher SFR/$M_{\rm star}$ than massive galaxies at low to intermediate redshift (i.e., "downsizing," e.g., Kauffmann et al. 2003; Heavens et al. 2004) might not necessarily mean relative scarcity of low-mass galaxies at high redshift. A significant fraction of old stars in relatively massive (e.g., $\sim 10^{11}$ $M_{\odot}$) galaxies at low redshift could be formed at high redshift in actively star-forming low-mass galaxies which had coalesced into more massive objects through the mergers. One of the means to address this is to investigate the distribution of the SFR and mean stellar age of galaxies as a function of stellar mass down to low mass at high redshift. The combination of the distribution of the SFR and mean stellar age as a function of stellar mass and the SMF shown in this study allows us to measure the contributions of galaxies in a certain mass range to the cosmic SFR density and stellar mass density and their age distribution as a function of redshift. We will be able to use these quantities in order to estimate what the mass range of high-z galaxies could have assembled into more massive galaxies at later epochs.

5. SUMMARY

In this paper, we have investigated the stellar mass function of galaxies at $0.5 < z < 3.5$, using the very deep and wide NIR imaging data obtained in MODS and the multiwavelength public data from the GOODS. The MODS data reach $K \sim 23$ over ~ 103 arcmin^2 and $K \sim 24$ over ~ 28 arcmin^2. We constructed a large sample of galaxies down to $\sim 10^9$–10^{10} $M_{\odot}$ up to $z \sim 3$.

Our main results are as follows.

1. The normalization of the SMF decreases with redshift gradually and the integrated stellar mass density becomes ~8%–18% of the local value at $z \sim 2$ and ~4%–9% at $z \sim 3$. The evolution of the stellar mass density estimated with the GALAXEV model is consistent with those in previous surveys.
2. The characteristic mass M^* of the best-fit Schechter function shows no significant evolution. With the Maraston model, however, M^* becomes smaller by a factor of ~ 2–2.5 at $z > 1.5$. This may be because many massive galaxies

are in active star-forming phase at $z > 1.5$ and TP-AGB stars would contribute to the SED of these massive galaxies significantly only at $z > 1.5$.

3. The low-mass slope of the SMF becomes steeper with redshift gradually from $\alpha = -1.29 \pm 0.03(\pm 0.04)$ at $0.5 < z < 1.0$ to $\alpha = -1.48 \pm 0.06(\pm 0.07)$ at $1.5 < z < 2.5$ and $\alpha = -1.62 \pm 0.14(\pm 0.06)$ at $2.5 < z < 3.5$. The evolution of the number density of low-mass (10^9–$10^{10}\ M_\odot$) galaxies is weaker than that of M^* ($\sim 10^{11}\ M_\odot$) galaxies. The contribution of these low-mass galaxies to the cosmic stellar mass density increases with redshift and becomes significant at $z \sim 3$.
4. We noted a marginal upturn around $\sim 10^{10}\ M_\odot$ and a steeper slope at $< 10^{10}\ M_\odot$ in the SMF. Shallow data, which does not reach to $< 10^{10}\ M_\odot$, could lead to underestimation of the low-mass slope.
5. The steepening of the low-mass slope with redshift could be explained as a result of the hierarchical merging process. Since the mass dependence of the SFR/$M_{\rm star}$ distribution seen in previous studies is expected to lead to the steepening of the low-mass slope with time, the opposite trend found in this study suggests that the hierarchical merging process was very important for the stellar mass assembly of relatively low-mass galaxies at $1 \lesssim z \lesssim 3$.

We thank an anonymous referee for very helpful comments. This study is based on data collected at Subaru Telescope, which is operated by the National Astronomical Observatory of Japan. This work is based in part on observations made with the *Spitzer Space Telescope*, which is operated by the Jet Propulsion Laboratory, California Institute of Technology under a contract with NASA. Some of the data presented in this paper were obtained from the Multimission Archive at the Space Telescope Science Institute (MAST). STScI is operated by the Association of Universities for Research in Astronomy, Inc., under NASA contract NAS5-26555. Support for MAST for non-HST data is provided by the NASA Office of Space Science via grant NAG5-7584 and by other grants and contracts. Data reduction/analysis was carried out on "sb" computer system operated by the Astronomical Data Analysis Center (ADAC) and Subaru Telescope of the National Astronomical Observatory of Japan. IRAF is distributed by the National Optical Astronomy Observatories, which is operated by the Association of Universities for Research in Astronomy, Inc., under cooperative agreement with the National Science Foundation.

REFERENCES

Arnouts, S., et al. 2007, A&A, 476, 137
Baldry, I. K., Balogh, M. L., Bower, R. G., Glazebrook, K., Nichol, R. C., Bamford, S. P., & Budavari, T. 2006, MNRAS, 373, 469
Baldry, I. K., Glazebrook, K., & Driver, S. P. 2008, MNRAS, 388, 945
Balogh, M. L., Christlein, D., Zabludoff, A. I., & Zaritsky, D. 2001, ApJ, 557, 117
Barger, A. J., Cowie, L. L., & Wang, W.-H. 2008, ApJ, 689, 687
Bell, E. F., & de Jong, R. S. 2001, ApJ, 550, 212
Berta, S., et al. 2007, A&A, 476, 151
Bertin, E., & Arnouts, S. 1996, A&AS, 117, 393
Bertone, S., De Lucia, G., & Thomas, P. A. 2007, MNRAS, 379, 1143
Borch, A., et al. 2006, A&A, 453, 869
Borys, C., Smail, I., Chapman, S. C., Blain, A. W., Alexander, D. M., & Ivison, R. J. 2005, ApJ, 635, 853
Bower, R. G., Benson, A. J., Malbon, R., Helly, J. C., Frenk, C. S., Baugh, C. M., Cole, S., & Lacey, C. G. 2006, MNRAS, 370, 645
Brammer, G. B., van Dokkum, P. G., & Coppi, P. 2008, ApJ, 686, 1503
Brinchmann, J., Charlot, S., White, S. D. M., Tremonti, C., Kauffmann, G., Heckman, T., & Brinkmann, J. 2004, MNRAS, 351, 1151
Brinchmann, J., & Ellis, R. S. 2000, ApJ, 536, L77
Bruzual, G., & Charlot, S. 2003, MNRAS, 344, 1000
Bundy, K., Ellis, R. S., & Conselice, C. J. 2005, ApJ, 625, 621
Bundy, K., Fukugita, M., Ellis, R. S., Targett, T. A., Belli, S., & Kodama, T. 2009, ApJ, 697, 1369
Calzetti, D., Armus, L., Bohlin, R. C., Kinney, A. L., Koornneef, J., & Storchi-Bergmann, T. 2000, ApJ, 533, 682
Capak, P., et al. 2004, AJ, 127, 180
Caputi, K. I., McLure, R. J., Dunlop, J. S., Cirasuolo, M., & Schael, A. M. 2006, MNRAS, 366, 609
Chapman, S. C., Blain, A. W., Smail, I., & Ivison, R. J. 2005, ApJ, 622, 772
Cohen, J. G. 2001, AJ, 121, 2895
Cohen, J. G., Hogg, D. W., Blandford, R., Cowie, L. L., Hu, E., Songaila, A., Shopbell, P., & Richberg, K. 2000, ApJ, 538, 29
Cole, S., et al. 2001, MNRAS, 326, 255
Conselice, C. J., Blackburne, J. A., & Papovich, C. 2005, ApJ, 620, 564
Conselice, C. J., et al. 2007, MNRAS, 381, 962
Cowie, L. L., Barger, A. J., Hu, E. M., Capak, P., & Songaila, A. 2004, AJ, 127, 3137
Daddi, E., Cimatti, A., Renzini, A., Fontana, A., Mignoli, M., Pozzetti, L., Tozzi, P., & Zamorani, G. 2004, ApJ, 617, 746
Daddi, E., et al. 2007, ApJ, 670, 156
Dawson, S., Stern, D., Bunker, A. J., Spinrad, H., & Dey, A. 2001, AJ, 122, 598
De Lucia, G., & Blaizot, J. 2007, MNRAS, 375, 2
Dickinson, M., Papovich, C., Ferguson, H. C., & Budavári, T. 2003, ApJ, 587, 25
Drory, N., & Alvarez, M. 2008, ApJ, 680, 41
Drory, N., Bender, R., Feulner, G., Hopp, U., Maraston, C., Snigula, J., & Hill, G. J. 2004, ApJ, 608, 742
Drory, N., Salvato, M., Gabasch, A., Bender, R., Hopp, U., Feulner, G., & Pannella, M. 2005, ApJ, 619, L131
Elsner, F., Feulner, G., & Hopp, U. 2008, A&A, 477, 503
Feulner, G., Gabasch, A., Salvato, M., Drory, N., Hopp, U., & Bender, R. 2005, ApJ, 633, L9
Fioc, M., & Rocca-Volmerange, B. 1997, A&A, 326, 950
Fontana, A., et al. 2003, ApJ, 594, L9
Fontana, A., et al. 2004, A&A, 424, 23
Fontana, A., et al. 2006, A&A, 459, 745
Franceschini, A., et al. 2006, A&A, 453, 397
Giavalisco, M., et al. 2004, ApJ, 600, L93
Glazebrook, K., et al. 2004, Nature, 430, 181
Grazian, A., et al. 2006, A&A, 449, 951
Gwyn, S. D. J., & Hartwick, F. D. A. 2005, AJ, 130, 1337
Heavens, A., Panter, B., Jimenez, R., & Dunlop, J. 2004, Nature, 428, 625
Hopkins, A. M. 2004, ApJ, 615, 209
Hopkins, A. M., & Beacom, J. F. 2006, ApJ, 651, 142
Ichikawa, T., et al. 2006, Proc. SPIE, 6269, 38
Ichikawa, T., et al. 2007, PASJ, 59, 1081
Ilbert, O., et al. 2009, arXiv:0903.0102
Jimenez, R., Panter, B., Heavens, A. F., & Verde, L. 2005, MNRAS, 356, 495
Juneau, S., et al. 2005, ApJ, 619, L135
Kajisawa, M., & Yamada, T. 2005, ApJ, 618, 91
Kajisawa, M., & Yamada, T. 2006, ApJ, 650, 12
Kajisawa, M., et al. 2006, PASJ, 58, 951
Kauffmann, G., et al. 2003, MNRAS, 341, 54
Khochfar, S., Silk, J., Windhorst, R. A., & Ryan, R. E., Jr. 2007, ApJ, 668, L115
Kitzbichler, M. G., & White, S. D. M. 2007, MNRAS, 376, 2
Kuchinski, L. E., Madore, B. F., Freedman, W. L., & Trewhella, M. 2001, AJ, 122, 729
Labbé, I., et al. 2005, ApJ, 624, L81
Leggett, S. K., et al. 2006, MNRAS, 373, 781
Madau, P. 1995, ApJ, 441, 18
Madau, P., Ferguson, H. C., Dickinson, M. E., Giavalisco, M., Steidel, C. C., & Fruchter, A. 1996, MNRAS, 283, 1388
Maraston, C. 2005, MNRAS, 362, 799
Maraston, C., Daddi, E., Renzini, A., Cimatti, A., Dickinson, M., Papovich, C., Pasquali, A., & Pirzkal, N. 2006, ApJ, 652, 85
Marchesini, D., et al. 2007, ApJ, 656, 42
Marchesini, D., van Dokkum, P. G., Förster Schreiber, N. M., Franx, M., Labbé, I., & Wuyts, S. 2009, ApJ, 701, 1765
Pannella, M., Hopp, U., Saglia, R. P., Bender, R., Drory, N., Salvato, M., Gabasch, A., & Feulner, G. 2006, ApJ, 639, L1
Papovich, C., Dickinson, M., & Ferguson, H. C. 2001, ApJ, 559, 620
Papovich, C., et al. 2006, ApJ, 640, 92
Pérez-González, P. G., et al. 2008, ApJ, 675, 234

Pozzetti, L., et al. 2007, A&A, 474, 443
Rawat, A., Wadadekar, Y., & DeMello, D. 2009, ApJ, 695, 1315
Reddy, N. A., & Steidel, C. C. 2009, ApJ, 692, 778
Reddy, N. A., Steidel, C. C., Erb, D. K., Shapley, A. E., & Pettini, M. 2006a, ApJ, 653, 1004
Reddy, N. A., Steidel, C. C., Fadda, D., Yan, L., Pettini, M., Shapley, A. E., Erb, D. K., & Adelberger, K. L. 2006b, ApJ, 644, 792
Rudnick, G., et al. 2003, ApJ, 599, 847
Rudnick, G., et al. 2006, ApJ, 650, 624
Ryan, R. E., Jr., et al. 2007, ApJ, 668, 839
Salpeter, E. E. 1955, ApJ, 121, 161
Sandage, A., Tammann, G. A., & Yahil, A. 1979, ApJ, 232, 352
Santini, P., et al. 2009, arXiv:0905.0683
Sawicki, M., et al. 2007, Deep. Astron. Surv., 380, 433
Schechter, P. 1976, ApJ, 203, 297
Scodeggio, M., et al. 2009, A&A, 501, 21
Shapley, A. E., Erb, D. K., Pettini, M., Steidel, C. C., & Adelberger, K. L. 2004, ApJ, 612, 108
Shapley, A. E., Steidel, C. C., Erb, D. K., Reddy, N. A., Adelberger, K. L., Pettini, M., Barmby, P., & Huang, J. 2005, ApJ, 626, 698
Springel, V., et al. 2005, Nature, 435, 629
Stringer, M. J., Benson, A. J., Bundy, K., Ellis, R. S., & Quetin, E. L. 2009, MNRAS, 393, 1127
Suzuki, R., et al. 2008, PASJ, 60, 1347
Taylor, E. N., et al. 2009, ApJ, 694, 1171
Treu, T., Ellis, R. S., Liao, T. X., & van Dokkum, P. G. 2005, ApJ, 622, L5
van Dokkum, P. G., et al. 2006, ApJ, 638, L59
Vergani, D., et al. 2008, A&A, 487, 89
Wang, W.-H., Barger, A. J., & Cowie, L. L. 2009, ApJ, 690, 319
Wilkins, S. M., Trentham, N., & Hopkins, A. M. 2008, MNRAS, 385, 687
Williams, R. E., et al. 1996, AJ, 112, 1335
Wirth, G. D., et al. 2004, AJ, 127, 3121